NTNU
Innovation and Creativity

# Automatic Intima-Lumen detection in Cardiovascular Ultrasound.

**Kristin Holm Edvardsen**

Master of Science in Communication Technology

| | |
|---|---|
| Submission date: | June 2006 |
| Supervisor: | Tor Audun Ramstad, IET |
| Co-supervisor: | Hans Torp, ISB |
| | Stein Inge Rabben, GE Vingmed Ultrasound |

Norwegian University of Science and Technology
Department of Electronics and Telecommunications

# Problem Description

An algorithm for automatic detection of the vessel wall in an ultrasound image has previously been developed. The aim of the thesis is to improve this algorithm by trying out alternatives to some of the cost-criteria in the algorithm; combining the gradient and std information in the image, and using a model matching criteria with 1.5 Gaussian curves.

The new algorithm is to be tested on a large number of datasets, and compared to the already existing algorithm, this by comparing both algorithms with manual measurement.

Helseundersøkelsen i Nord-trøndelag (HUNT) is studying endothelial function in Brachialis by manually tracking the vessel wall at end-diastole and measuring the vessel diameter from this. Trying out the automatic vessel detection algorithm on Brachialis ultrasound recordings will be part of the thesis.

Assignment given: 16. January 2006
Supervisor: Tor Audun Ramstad, IET

# Abstract

The main goal in this thesis has been to develop an algorithm that robustly identifies the Carotid artery wall boundaries throughout a heart cycle in an ultrasound image. An existing automatic vessel detection algorithm (AVDA) uses tissue velocity imaging(TVI) and B-mode data to score candidate points from various criteria. The candidate pair with the lowest score gets selected.

AVDA was extended by implementing two alternative criteria to the existing external cost criterion. The first by combining the information on gradient and standard deviation in the intensity signatures; the GradTrans criterion (GTC).The second by exploiting the shape of the intensity signature across the vessel wall in the detection of the intima-lumen interfaces and using a Model Matching criterion with 1.5 Gaussian curves (MMC1.5).

An edge criteria modeling tool (ECMT) was developed for the purpose of studying the intensity signatures across the vessel wall to find out how the various cost criteria score the signatures of different datasets. In addition, the ECMT was used for parameter tuning. The implemented criteria were verified by comparing automatically detected edges with manual detected edges on 22 datasets. In addition automatically detected vessel diameter was compared against manually detected diameter on 49 datasets. The verification indicated that the GTC is not a good criterion for detecting the intima-lumen interface. The GTC either completely failed to detect the wall or detected the media-adventitia boundary instead of the intima-lumen boundary.

The MMC1.5 criterion, on the other hand, seems promising. The criterion seems to often detect the wall correctly or with a small deviation. Compared with manual diameter measurement, MMC1.5 had a bias of 0.014 mm and *std* of the error was 1.056. In some images the criterion failed completely in correct detection of the wall. The reason being that a similar structure in the wall or an artifact in the lumen was detected instead. After removing these outlays, the diameter detection by MMC1.5 had a bias of 0.146 mm and *std* of 0.347 mm. The criterion has to be developed further to be more robust and less time consuming, and to overcome the problems of complete failure.

A feasability study was done to see whether the AVDA can be used on Brachialis recordings to increase the efficiency of the Flow Mediated Dilation measures. The study seems promising when using the Gradient criterion. This makes it possible to automatically measure diameter changes throughout a heart cycle as well as measuring the differences in diameter between recordings.

# Preface

This report documents my work on the final master thesis. The thesis completes my Master of Technology degree in Communication Technology at the Norwegian University of Science and Technology, Faculty of Information Technology, Mathematics and Electrical Engineering, Department of Electronics and Telecommunications. The work was carried out at the Department of Circulation and Imaging under the supervision of professor Hans Torp and Stein Inge Rabben, PhD. I would like to thank both of them for their help and support. I would also like to thank professor Patrick Segers and his department at Gent University for an inspiring stay, and for helpful feedback on my work.

Further I would like to thank my fellow students at the department for making this a positive final year and finally I thank my happy little family, Julie and Christian for their support and inspiration.

Trondheim, June 26, 2006

Kristin Holm Edvardsen

# Contents

# Abbreviations

| | |
|---|---|
| **US** | Ultrasound |
| **IMT** | Intima Media Thickness |
| **AVDA** | Automatic Vessel Detection Algorithm |
| **MMC2** | Model Mathing Criterion with 2 Gaussian curves |
| **MMC1.5** | Model Mathing Criterion with 1.5 Gaussian curves |
| **GTC** | GradTrans Criterion |
| **ECMT** | Edge Criteria Modelling Tool |
| **TVI** | Tissue Velocity Imaging (Tissue Doppler) |
| **LUT** | Look Up Table |
| **PSF** | Point Spread Function |
| **ROI** | Region Of Interest |
| **STD** | Standard Deviation |
| **M&A** | Measurement and Analysis |
| **FMD** | Flow Mediated Dilation |
| **RF** | Radio Frequency |
| **TGC** | Time Gain Compensation |
| **IQ** | In-phase Quadrature |
| **DP** | Dynamic programming |
| **RF** | Radio Frequency |
| **SNR** | Signal to Noise Ratio |
| **PSF** | Point Spread Function |
| **HUNT** | Helseundersøkelsen i Nord-Trøndelag |

# 1 Introduction

Cardiovascular diseases are dominating causes for sickness and death among elderly people [34]. Endothelial dysfunction is thought to be an important factor in the development of atherosclerosis, hypertension and heart failure [10]. Changes in arterial stiffness increases with age, and in disorders such as hypertension and diabetes. Studies have shown that there is a relation between large arterial stiffening and impairment of cardiac function, like ventricular systolic stiffening [8], [26] and [27]. By measuring the exact intima-lumen boundary throughout a heart cycle, one will get an exact measure of the lumen diameter as a variation of time. Measuring the inner diameter of the vessel throughout a heart cycle using ultrasound provides an easy way to assess artery stiffness measurements [27], and can therefore be used in cardiac disease risk assessment.

Atherosclerosis in coronary vessels are often the underlaying causes of coronary diseases. The development of atherosclerostic plaque causes the media layer to thicken, growing into the lumen. This causes the diameter of the vessel to decrease and hence a reduction in the blood supply, as well as carrying the risk of plaque rupture that might cause myocardial infarction [4], [21]. Intima media thickness (IMT), the thickness of the tunica intima and tunica media, is considered to be a marker for early atherosclerosis [6]. Measurement of IMT in the Common Carotid can detect morphological change in the vessel wall, and hence be used to predict cardiovascular events. IMT is used for assessing the structural changes of the vessel caused by for example high blood pressure.

Manual tracing of the vessel wall was long the main detection method. This gives potential limitations in reproducibility due to ultrasonographer dependence. Another drawback is that manual measurement is time consuming. Researchers have developed various automatic methods for detecting the vessel wall in vascular and intravascular ultrasound, [7], [9], [13], [20], [19]and [23]. Candidate points are associated with a composite cost function, where constraints are put on the contour shape to assure geometrical smoothness (internal cost), and the characteristics of the image features in the neighborhood (external cost). Traditionally, external cost function is computed from the image gradient, which is very sensitive to image noise, and in addition, does not detect the lumen-intima, but the media-adventitia border.

An automatic vessel detection algorithm (AVDA) for detecting the wall edged in a vascular ultrasound image has been developed by Rabben [23]. This method has the same structure as a method made for detecting and tracking the apex and two landmarks defining the atrioventricular plane in apical views of the left ventricle described in [29]. Sets of candidate points are tracked within the selected RF Region of Interest (ROI). TVI and gray scale data are used to score the various candidate points from cost criteria based on the characteristic behavior and shape of the vessel. The candidate pair with the lowest cost is selected.

The key goal of this thesis is to define a cost function with better robustness and accuracy, and with less computational and manual initialization than the existing cost functions. An edge detection criterion using gradient and *std* information is implemented, based on the method presented by Luo et al. [20] and a method proposed by Rabben [24].

In the pre-project, autumn 2005, [12] the AVDA was extended with a model matching criterion with two Gaussian curves (MMC2). The MMC2 algorithm is time consuming and it is not robust enough, hence one goal of the thesis is to improve these deficiencies. This is done by developing a model matching method that utilizes the known shape of the intensity profile across the vessel wall better than the MMC2, in the detection of the wall boundaries. The proposed model is composed of a linear combination of one and a half Gaussian curves, where the one curve represents the intima layer and the half curve represents the slope of the adventitia layer. The algorithm will therefore only work on ultrasound images with visible intima-layers.

The new algorithms will be tested on a large number of datasets, and compared to manual detection for verification.

Helseundersøkelsen i Nord-trøndelag (HUNT) is studying endothelial function in Brachialis by manually tracking the vessel wall at end-diastole and thereafter measure the vessel diameter. A feasability study will be done to see whether the AVDA algorithm could improve the efficiency of the flow mediated dilation analysis, by automatic calculations of vessel diameter measurement.

This thesis is organized as follows. First, the theory chapter gives a description of the anatomy of the Common Carotid artery and a brief introduction to ultrasound imaging, followed by an explanation of the AVDA that this thesis is based on, and finally a presentation of other vessel edge detection methods. The Materials and Methods chapter describes the methods used in this thesis. The Results chapter provides the achieved results and the Discussion chapter presents an evaluation of the results. Finally a chapter with conclusion and proposals for further work.

# 2 Theory

This chapter provides the theoretical background for the thesis. First, a brief description of the anatomy of the Common Carotid artery. Second, an introduction to ultrasound imaging. Finally, a presentation of the vessel detection method that this thesis builds on, before a presentation of existing automatic/semi-automatic methods for vessel wall detection with focus on the external energy cost function.

## 2.1 Anatomy

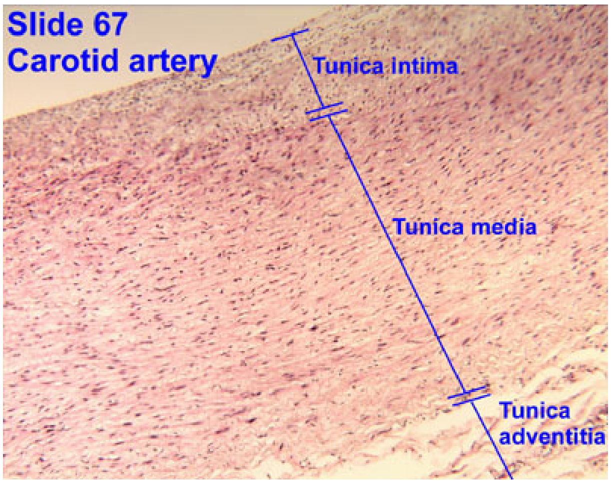

**Figure 1:** Anatomical picture of Common Carotid artery wall. Picture taken from [32].

Blood vessels are usually composed of three layers: the tunica intima, tunica media, and tunica adventitia. The tunica intima consists of a layer of endothelial cells lining the lumen of the vessel, as well as a subendothelial layer made up of mostly loose connective tissue. Often, the internal elastic lamina separates the tunica intima from the tunica media. The tunica media is composed mainly of circumferentially arranged smooth muscle cells. Again, the external elastic lamina often separates the tunica media from the tunica adventitia. Finally, the tunica adventitia is primarily composed of loose connective tissue made up of fibroblasts and associated collagen fibers [32]. Figure 1 shows an anatomical picture of the Common Carotid vessel wall, where the various layers are marked.

Endothelial dysfunction is thought to be an important factor in the development of atherosclerosis, hypertension and heart failure. Finding the intima-lumen boundary for both the upper and lower walls will give the inner diameter of the vessel. This can be used in estimation of the arterial wall stiffness and in estimating Flow Mediated Dilation (FMD), a technique used when studying endothelial dysfunction [10]. Intima media thickness (IMT), the thickness of the tunica intima and tunica media, expressed as a single measurement (in millimeters) or a rate of change (in millimeters per year), has been a good indicator of the presence and extent of coronary artery disease. IMT can be used to predict major cardiovascular events such as myocardial infarction and stroke [16].

## 2.2 Ultrasound imaging

If nothing else is stated, the information presented in this section is taken from [1], [2] and [17].

Ultrasound imaging, also called sonography, is a mode of medical imaging. It has become a popular mode for medical imaging, the reason being that the pictures can be taken with no surgical intervention, the apparatus is cheap and portable compared to other imaging modes like CT or MR, and there are no known serious side effects. Ultrasound is a soft-tissue modality, it gives good images of tissue and blood, however, it does not give useful images of or through bone or bodies of gas, such as the lungs and bowel.

### 2.2.1 Ultrasound imaging system

High frequency sound pulses are transmitted from an array of piezoelectric elements into the body. The pulse propagates through the body and echoes, reflected from structures in tissues and bone, are received by the transducer and processed for visualization. The time from pulse transmission till the echo is received, gives the distance to the reflecting area.

The impulse response of an ultrasound system during interrogation of an ideal point target is known as the system's point spread function (PSF) as it represents the spread of a point object in the image. The character of the PSF in the axial direction is determined by the center frequency and bandwidth of the acoustic signal generated at each transducer element. The lateral and elevation dimensions character is determined by the aperture and element geometries as well as the beam forming applied.

When an ultrasound pulse encounters a boundary between two tissue structures, the pulse will be partially reflected and partially transmitted. The reflection depends on the difference between the characteristic impedances of the two materials. The characteristic impedance is defined as $Z = \rho c$, where $\rho$ is the mass density of the material and $c$ is the sound velocity in the material. Reverberations are caused by multiple reflections, meaning that the pulse bounces back and forth between structures. This sometime causes artifacts where it seems that a structure is placed further into the body, behind the actual structure.

As the pulse propagates through the tissue, the intensity is attenuated due to power absorption, scattering losses and geometric spread. This causes the reflections from far targets to be weaker than the reflections from near targets. This is compensated for by using a time variable gain.

The ability of an ultrasound system to discriminate closely spaced scatterers is specified by its spatial resolution. The radial resolution, $\Delta r$, is proportional to the wavelength, $T_p$, and hence inversely proportional to the bandwidth, $B$. $\Delta r = cT_p/2 = c/2B$. The higher the frequency, the better the resolution, but unfortunately, attenuation of the pulse also increases with frequency. The lateral resolution, $\Delta l$, is dependent on the relationship between the wavelength and the size of the probe. $\Delta l = \lambda F/D$, where F is the depth and D is the beam width, i.e the diameter of the array aperture.

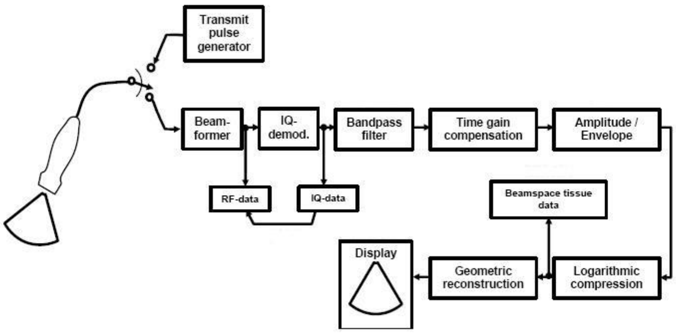

**Figure 2:** Block diagram of a typical ultrasound imaging system. Figure taken from [31].

Figure 2 illustrates the various parts of an ultrasound imaging system. The output of the beamformer is the received Radio Frequency (RF) signal. It contains frequency information in the frequency bands used, and is a notation for unprocessed data in the ultrasound industry. The RF signal is in-phase quadrature (IQ) demodulated, a technique used to extract the amplitude and phase information in a signal, this to reduce the amount of data without loosing the essential information [18]. Next, the signal is bandpass filtered to increase the signal to noise ratio (SNR). To compensate for the attenuation of the signal as it propagates through tissue, time gain compensation (TGC) is used to amplify the signal. Amplitude and envelope detection is then used to rectify and smooth the signal. Finally the signal is logarithmic compressed to get better contrast, before it gets scanconverted and displayed on the screen [31].

### 2.2.2 K-space

The Fraunhofer approximation states that the far-field complex amplitude pattern produced by a complex aperture amplitude function is approximately equal to the 2-D Fourier transform of that function, meaning that in ultrasound the ultrasound beam's pressure amplitude pattern can be estimated by taking the 2-D Fourier transform of the transducer aperture.

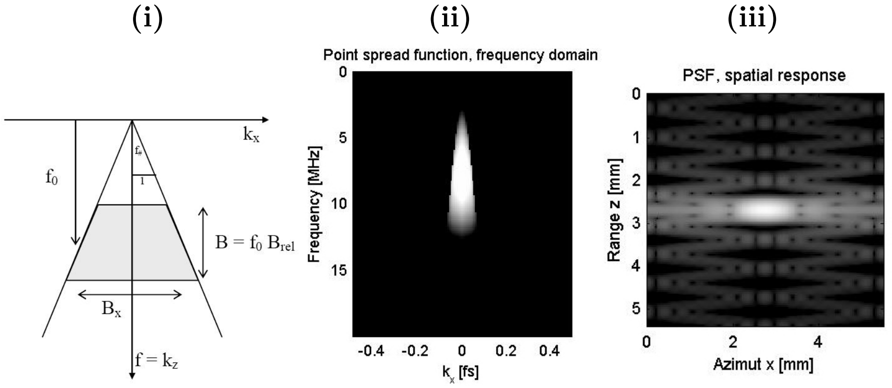

**Figure 3:** (i) $B$ is double sided bandwidth in Hz, $B_x$ is the bandwidth in the $k_x$ direction, $B_{rel}$ is relative bandwidth $B_{rel} = B/f_0$, $a$ is aperture in meter, $R$ is the focal distance, $\lambda$ is wavelength in meter, $f_\#$ is the F-number ($f_\# = R/a$).(ii) shows the PSF in the frequency domain, while (iii) show the PSF in the spatial domain. Figures are taken from [30].

K-space is a two-dimensional frequency space. It is a linear system approach to the Fraunhofer approximation, and can thus only be applied under conditions of linear propagation and within the constraints of that approximation. K-space analysis is a method for using the spatial frequency domain representation of ultrasound system impulse response and scattering functions, to understand and analyze imaging methods.

Figure 3 illustrates the geometry of the PSF in frequency domain in (i) and (ii), and the PSF in the spatial domain in (iii). The PSF in (ii) is the product of the aperture frequency response and the pulse frequency response.

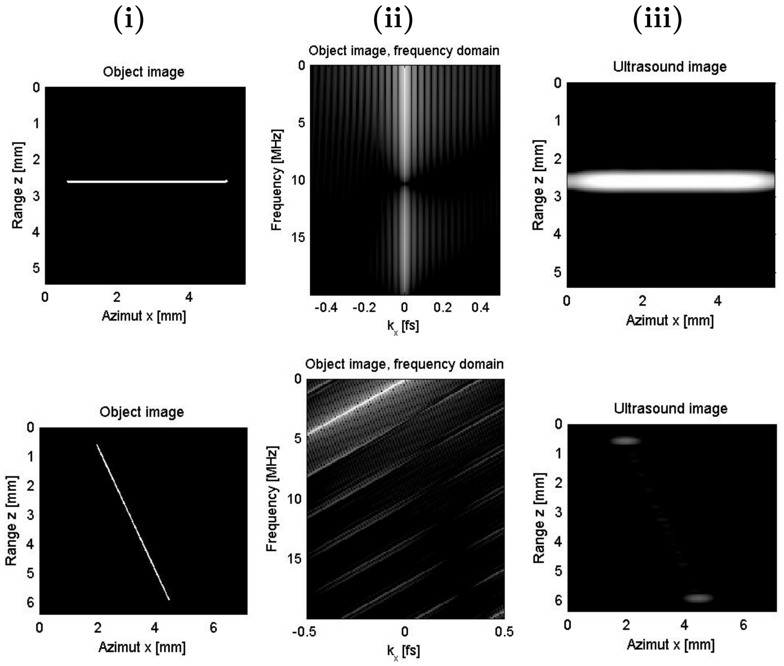

**Figure 4:** K-space evaluation of a horizontal line, and a line with an incline larger than the critical angle. (i) shows the original images, (ii) the original images in frequency domain and (iii) shows the ultrasound images.The PSF used here is the same as in figure 3. Figures are taken from [30].

A thin horizontal line will show up as a vertical line in k-space (upper pictures in figure 4). As the angle between the line and the horizontal plane increases (lower pictures in figure 4), the thin line will get weaker and disappear at an angel of $arctan(2/f_{\#})$ as it will be outside the PSF in the frequency domain.

### 2.2.3 Imaging modes

This section describes the imaging modes used in this thesis.

**B-mode**

Brightness mode, presents the viewer with gray-scale image. The geometry of the scanned area is visualized, using brightness to map the echo amplitude after TGC. B-mode is based on transmitting on one frequency and receiving on the second harmonic frequency, 2nd harmonic imaging.

**Tissue Velocity Imaging (TVI)**

TVI is performed by sweeping the ultrasound beam across the selected region of the vessel, while estimating the tissue velocity in several ranges along the beam. TVI uses an autocorrelation technique to calculate the velocities. The velocity information is usually displayed as color-coded segments superimposed on the gray-scale B-mode image. The sampling frequency used is called the pulse repetition frequency (PRF), PRF = 1/PRT. To avoid frequency aliasing, the Doppler shift ($f_d$) must be according to the Nyquist criterion, less than half the PRF ($f_s$); $f_d < f_s/2$.

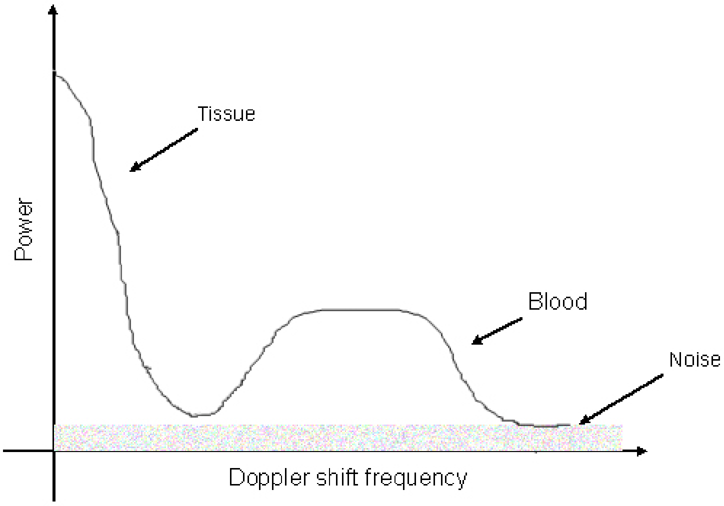

**Figure 5:** Illustrating the difference in power received from the moving wall to that of the blood.

TVI maps the tissue velocity rather than the blood velocity. The velocity of the vessel wall is considerably lower (0-15 cm/s) than the velocity of the blood flow. As illustrated in figure 5, the Dopplersignal received from the moving vessel wall has much higher power (approximately 40dB higher) than the signal received from blood flow, thus noise from blood signals is negligible [15]. Additionally, as the beam is almost perpendicular to the blood flow direction, there will be little Doppler signal received from the blood flow compared to the signal from the vessel wall, which moves along the ultrasound beam.

When recording TVI data and B-mode simultaneously, the total frame rate has to be scheduled between these two tasks. A high framerate is necessary in the TVI data to prevent frequency aliasing. This is done

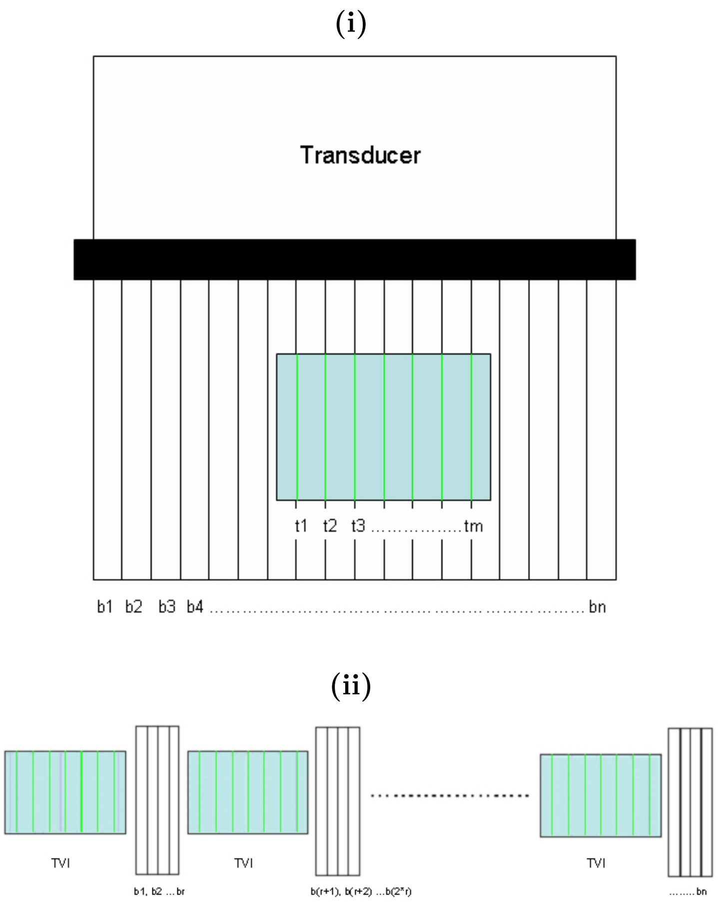

**Figure 6:** Illustration of simultaneous recording of B-mode (large rectangle) and TVI (the green rectangle) (i), and the transmit sequence for TVI data and B-mode.

by recording the B-mode in between the Doppler pulses, as illustrated in figure 6. A whole IQ image is recorded, then parts of the B-mode image, before a new whole IQ image is recorded, before another part of the B-mode image. This gives a higher frame rate for the IQ image than for the tissue image. This is illustrated in figure 7, showing the position of the posterior wall throughout the heart cycles, the resolution on the TVI data (blue line) is much higher than that of the tissue data (red crosses).

### 2.2.4 Imaging the vessel wall

A linear array probe is used when imaging the Common Carotid. This gives a rectangular format with the same width both in the near and far field.

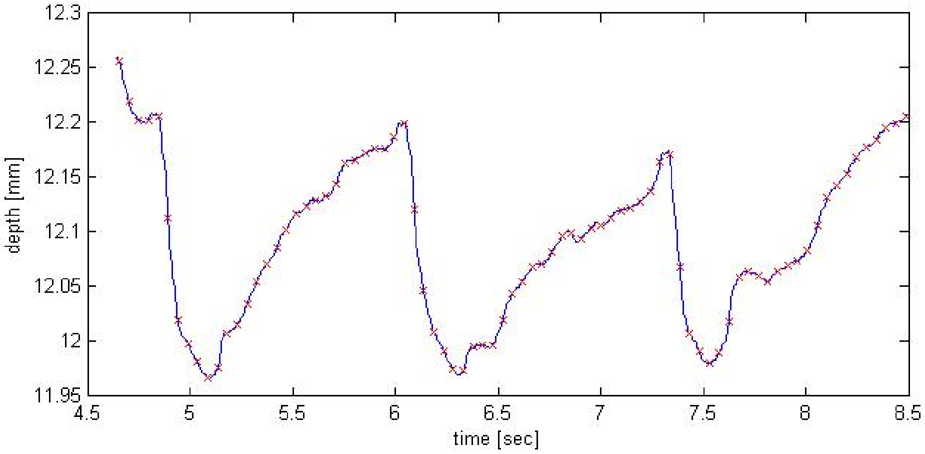

**Figure 7:** Plotting the position of the posterior vessel wall throughout the heart cycles. The blue line represents the RF data, whereas the red crosses represents the tissue data.

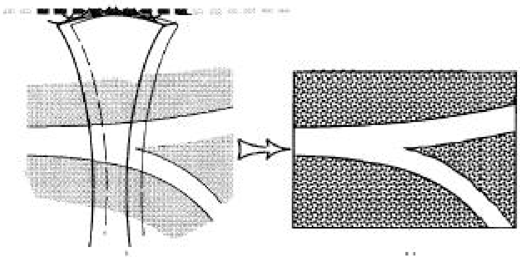

**Figure 8:** Scanning the Carotid using a linear probe (left) and the resulting ultrasound picture (right). The figure is taken from [2].

When imaging the Common Carotid, we have shallow imaging, hence high frequency can be used. This will give a good enough radial resolution to differentiate between the various layers of the vessel wall.

The anterior and posterior walls have two echogenic lines separated by a hypoechoic space. The inner line corresponding to the lumen-intima interface and the outer to the media-adventitia interface, while the hypoechoic space corresponds to the media layer [33]. Because the tunica intima is a very thin layer with lined scatterers, the width of the inner echogenic line is related to the pulse length. As the adventitia layer is a summation of many scatterers at different depths, the width of the echo from adventitia is variable. A grayscale ultrasound image of the Carotid is seen in figure 9

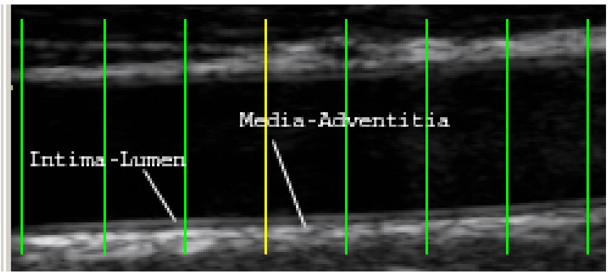

**Figure 9:** Image showing a grayscale image of the Carotid with indications on the intima-lumen and media-adventitia boundaries.

When recording the ultrasound images of the vessel, it is necessary to place the probe at an angle less than the critical angle to the vessel, to be able to receive the echo and view the intima layer (as explained in 2.2.2). If the angle is larger than the critical angle, the echo will be reflected in another direction than the transducer. Another issue is that the plane must be placed in the middle of the vessel to be able to see the intima layer. This is also important to be able to detect correct vessel diameters.

Ringing is caused by the transducer being in resonance after having removed the voltage source. Because of this ringing, the pulse has a tail. Reverberations in adventitia expands the pulse and makes the extension longer. This pulse tail causes the trailing edge (intima-lumen boundary) on the anterior vessel wall to be less distinct than the leading edge of the posterior wall. This can be seen in figure 10.

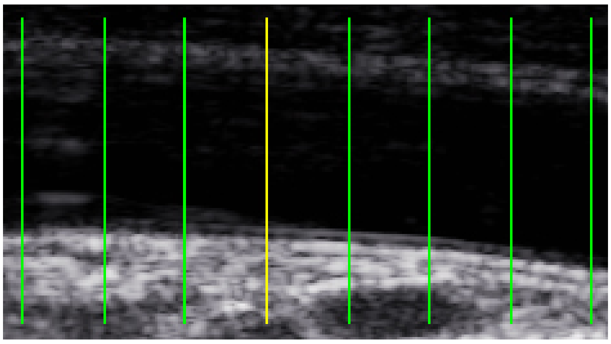

**Figure 10:** Image illustrating how the pulse tail causes the anterior wall edge to be less distinct than the posterior wall edge.

As the intima layer is not always visible in different subjects, it is important to be consistent when recording and measuring. Either the diameter measures must be on anterior media-adventitia to posterior media-adventitia or on anterior intima-media to posterior intima-media. Inner and outer diameter measurements are not comparable as they give different diameter measures and diameter distention measures of the wall thickening.

## 2.3 Vessel edge detection

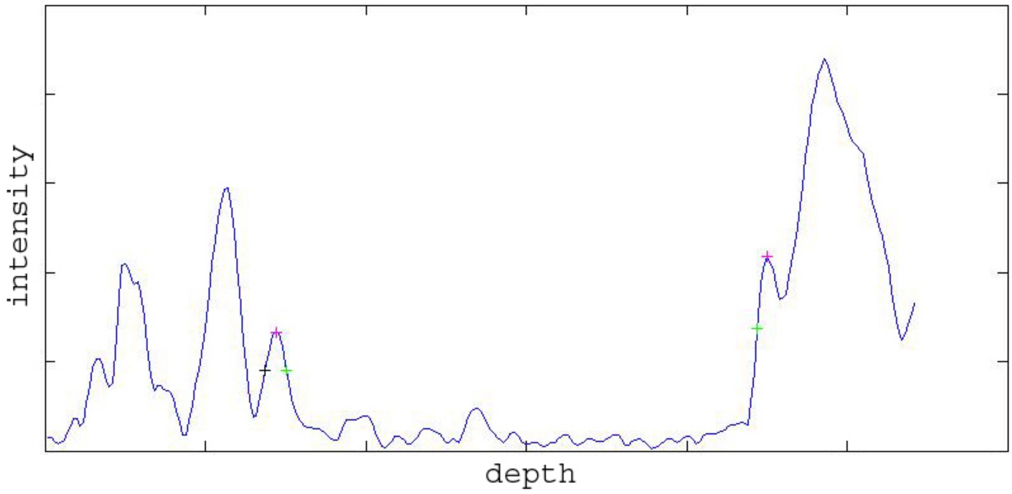

**Figure 11:** Illustrating edge positions along one intensity beam. The pink crosses represents actual border crossing. The green crosses represents the visual border in the ultrasound images. The black cross represents the leading edge in the anterior wall.

When the observers detects the intima-lumen boundary in an ultrasound image, the visual boundary in the image is detected, corresponding to the green crosses in the plot in figure 11. This, however, is not the true boundary between intima and lumen. The actual boundary is the peak of the intima-curve, represented by the pink crosses. This gives an underestimation of the inner diameter. The underestimation equals the width of the intima-curve, which is one pulse length. Some researchers, [13] and [19], solves this by detecting the leading edge on both the anterior and posterior wall (black cross in anterior wall to green cross in posterior wall in the figure). The leading edge of the intima-lumen boundary in the anterior wall is more difficult to detect, and this might also be confusing for the operators as they are used to manually detecting the trailing to leading edge, which visually seems to be the edges. In this thesis, the visual borders, represented by the green crosses, are detected.

The points within the RF-ROI are all vessel wall candidate points. Each candidate point, $c(i)$ is associated with a composite cost function according to the characteristics of the formation of the boundary, where constraints are put on the contour shape to assure geometrical smoothness (internal cost, $C_{int}$), and the image features in the neighborhood (external cost, $C_{ext}$) [22], [20], [19].

$$C(c_1, ..., c_n) = \sum_{j=1}^{n} C_{ext}(c_j) + \sum_{j=2}^{n} C_{int}(c_j, c_{j-1}) \tag{1}$$

Traditionally the external cost gets computed from the image gradient. In the following sections, other methods for computing the external cost will be presented. The automatic vessel detection algorithm developed by Rabben [23] is described in the subsection below. Thereafter a study of other existing methods for vessel boundary detection is presented.

### 2.3.1 The Automatic Vessel Detection Algorithm (AVDA).

In [29] a method for detecting and tracking the apex and two landmarks defining the atrioventricular plane in apical views of the left ventricle is described. The ideas from this method was used in the development of an algorithm for vessel wall detection, done by Rabben [23]. The method is the same, scoring each candidate pair and then selecting the candidate pair with the lowest score, but the criteria for calculating the costs are modified to fit the characteristic behavior and shape of a vessel.

Initially the candidate points ($c_i$) are positioned with an adequate resolution along the beams in the ROI. Using the TVI data the candidate points are tracked throughout all the ultrasound frames in a cardiac cycle according to the displacement estimator described in appendix A.1 [25]. Next, the timeframes in the TVI data where there exists grayscale data are found, see figure 7. A candidate point is given a cost ($C$) based on a set of cost functions ($C_j$) described below. The cost functions consists of three components:

$$C_j(c) = w_j M_j(B_j(c)) \tag{2}$$

Where $M_j$ is a mapping function that maps the function in a way that good candidates are given a low cost, $B_j(c)$ is based on the characteristics of the candidate point and $w_j$ is a weight giving each cost function a relative importance compared to other cost functions. Most of the cost functions use the mapping $M_{exp(x)} = ax^b$. This mapping is controlled by $a$ and $b$, which are given by defining two points which specify the normal range. The first

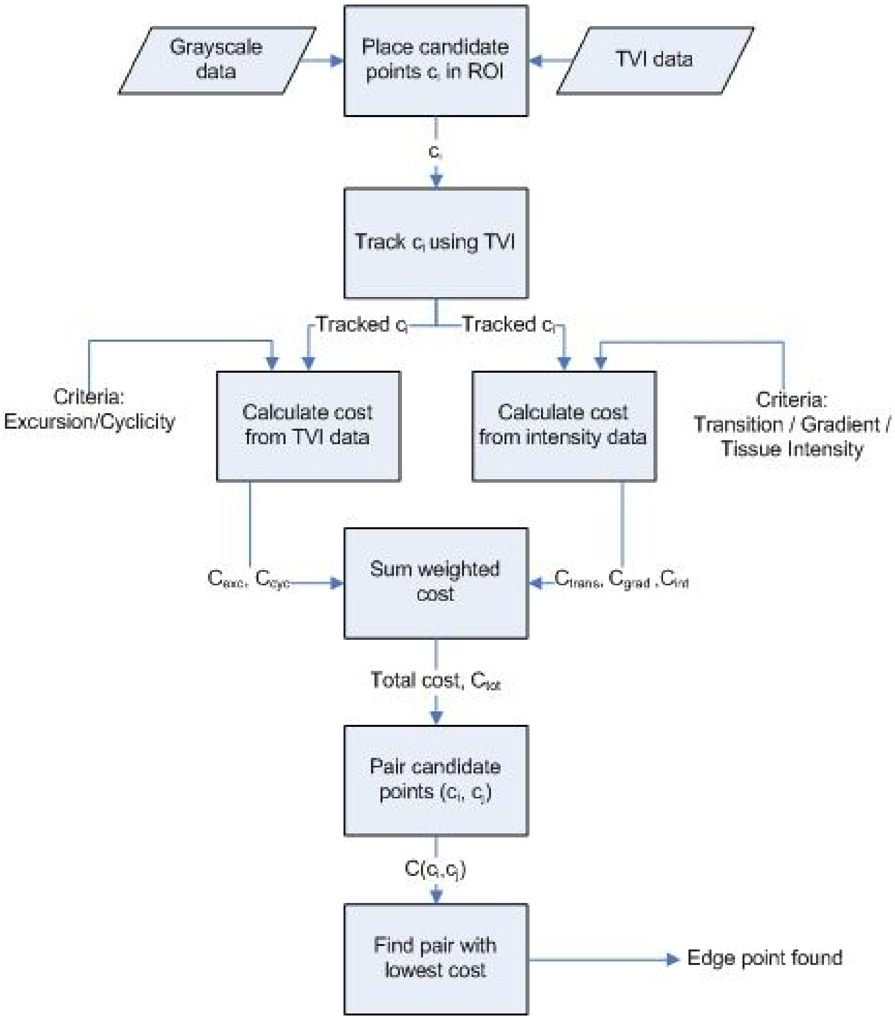

**Figure 12:** Flow chart of the AVDA.

point, $(x_1, y_1)$ specifies a low value and the second point, $(x_2, y_2)$, specifies the unit value. $a$ and $b$ are given by $b = (log(y_1)-log(y_2))/(log(y_1)-log(y_2))$ and $a = y_2/x_2^2$ [29].

For all the frames, the cost for each candidate point is computed from various characteristics of the vessel wall [29]. The internal cost terms excursion and cyclisity are computed from TVI data, and the external cost terms tissue intensity, blood-tissue transition and spatial gradient are computed from gray scale data. The various cost terms are normalized to the range [0,1] by their respective maximum values in the whole image.

Excursion: Excursion is defined as the maximal displacement (difference between the maximum depth and minimum depth) of a material point through one heart cycle. The inner layer of the arterial wall moves fastest and hence has the highest excursion. Blood is flowing fast and might have higher excursion than possible tissue excursions and must therefore be be given a high cost. Also values lower than the tissue displacement must be given high costs. The excursion cost is assigned to a candidate point by:

$$C_{exc}(c_i) = M_{exp}(max_n(d_i(n)) - min_n(d_i(n))) \tag{3}$$

Where $d_i$ is depth. The cost function is exponential outside the range of reasonable tissue excursion and low within the reasonable tissue excursion range.

Cyclicity: Unless there is respiration artifacts, the vessel wall will return to its original position after one heart cycle, it is cyclic. Cyclicity cost is computed as the distance between the start and end position of one point through a heart cycle:

$$C_{cyc}(c_i) = M_{exp}(abs(d_i(1)) - abs(d_i(N)))) \tag{4}$$

Where $N$ is the last frame in the heart cycle and $d_i$ is depth.

Transition:

Blood-tissue and tissue-blood transition can be calculated from either what is called transition cost or from gradient cost. Only one of these two cost functions are in use at one time. For both methods, a window is slid across the boundary intensity signatures of the US image, where the middle point of the window represents the candidate point. The average intensities of the left and right side of the window are calculated. A cost for blood-tissue transition is calculated, as well as one for tissue-blood transition. When finding the anterior wall, tissue-blood transition must be used, and when finding the posterior wall, blood-tissue transition must be used. Only blood-tissue transition cost calculation is explained here.

Transition cost is defined as the difference between the signature within the window and the computed averages [22]. The transition cost is proportional to the striped areas in figure 13.

$$C_{trans}(c_i) = \sum_{j=1}^{m} V(p_j)^2 - c_i^2 - \frac{\left( (\sum_{j=1}^{k-1} V(p_j))^2 + (\sum_{j=k+1}^{m} V(p_j))^2 \right)}{m} \tag{5}$$

Where $V(.)$ represents the gray scale value of a given pixels, p represents the pixels within the window, m is the length of the window, and k is the index of the middle point.

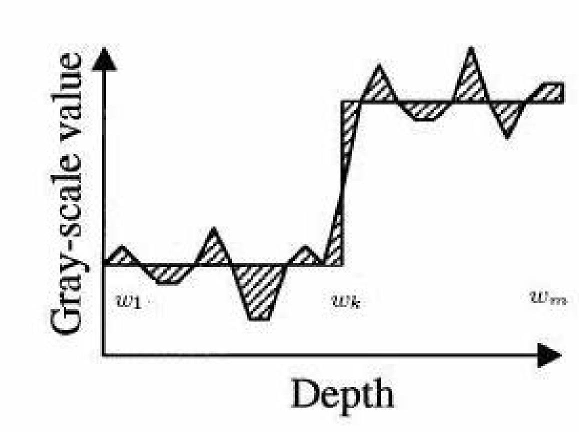

**Figure 13:** Illustration of the transition cost. The cost is proportional to the striped areas. $w_k$ is the candidate point and the horizontal lines are the left and right averages. Figure is a modified version of figure 4 in [22]

Gradient cost is defined as the average of the left side of the window minus the average of the right side. This is minimized when the jump in intensity from left to right is highest [22].

$$C_{grad}(c_i) = \frac{(\frac{1}{k-1}\sum_{j=1}^{k-1} V(p_j) - \frac{1}{m-k-1}\sum_{j=k+1}^{m} V(p_j) + V_{max})}{2V_{max}} \tag{6}$$

Where $V(.)$ represents the gray-scale value of a given pixel, $V_{max}$ is maximum gray-scale value of the imaging system, p represents the pixels within the window, m is the length of the window, and k is the index of the middle point.

The cost for blood-tissue transition, $C_{ext}$ is either computed from $C_{trans}$ or $C_{grad}$, where $w_{trans}$ is 1 or 0.

$$C_{ext}(c_i) = w_{trans} * C_{trans} + (1 - w_{trans}) * C_{grad} \tag{7}$$

Tissue intensity: The tissue intensity is normally highest in the media-adventitia interface. This can be used for finding the vessel wall, but not for measuring the exact lumen-intima interface. Tissue cost is defined as the normalized average tissue intensity:

$$C_{int}(c_i) = M_{exp}(255 - avg_n(p_i(n))) \tag{8}$$

As the intensity is highest somewhere in the adventitia layer, the weighting of tissuecost is normally set to zero as the aim is to find the lumen-intima interface.

Finding total cost: The costs are averaged over all the frames, finding a mean cost for each candidate point. To find the total cost for one point, the weights of the various costs are multiplied with the costs and then summed together.

$$C_{tot}(c_i) = w_{exc} * C_{exc}(c_i) + w_{cyc} * C_{cyc}(c_i) + w_{ext} * C_{ext}(c_i) + w_{int} * C_{int}(c_i) \tag{9}$$

Where $w_{exc}$, $w_{cyc}$, $w_{ext}$ and $w_{int}$ are the weights for the various costs, $w_{int}$ is normally set to zero.

Finding the candidate pair: Points that are separated by a physiological reasonable distance are paired together and the pair of points with the lowest total cost is selected as the vessel wall edge points.

$$C(c_i, c_j) = C_{tot}(c_i) + C_{tot}(c_j) \tag{10}$$

$$C_{edgePoints} = min(C(c_i, c_j)) \tag{11}$$

### 2.3.2 Existing vessel wall algorithms

A literature study was done to study various forms of computing the external cost.

#### 2.3.2.1 Combining maximum slope with thresholding

Chintio et al. [9] presents an algorithm for finding the imtima-lumen interface by finding the maximum slope of the intensity signal. First, the vessel is demarcated within the ROI by finding the maximum intensity in the posterior and anterior side. Next, the vessel wall is roughly detected by finding the maximum slope of each wall in the envelope signal. Thereafter, the positions of the intima-lumen interface is found by finding an intersection between a threshold and the envelope in the middle of the found positions of each wall and the lumen. The resolution is improved by solving the equation of a line between the two points laying closest to the threshold values of the anterior and posterior wall. The method underestimates the inner diameter.

#### 2.3.2.2 Combining multiple measurements of echo intensity, edge strength and edge continuity

Gustavsson et al. [13] describes a dynamic programming procedure for detecting the various layers in the carotid vessel wall; using local measurements of vessel echo intensity, edge strength and continuity to compute a cost function. The algorithm was created to overcome problems with weak echoes, echo dropouts and speckle noise that is often present in B-mode ultrasound imaging.

The various costs are defined for the posterior media-adventitia interface only; but the definitions for the anterior and posterior lumen-intima interface are of a similar nature. The cost function is composed of the echo intensity below the interface $c_1$, the intensity gradient in downward direction $c_2$ and the boundary continuity $c_3$. The echo intensity below the interface, $c_1$, is represented by the normalized average intensity of eight pixels beneath the candidate point $b_i$. $c_1$ is similar to transition cost described in section 2.3.1, except it looks only in half the window. The intensity gradient in downward direction, $c_2$, is the normalized value of estimated vertical intensity slope of a rectangular 5x5 neighborhood of the point $b_i$. This gives a lateral averaging. The boundary continuity, $c_3$, where $d_y$ is the change in vertical distance between the boundary being detected and a smooth reference boundary. This utilizes the information from candidates in neighboring beams to find the edge. $c_3$ is a part of the dynamic programming procedure.

#### 2.3.2.3 Local measurements of the echo intensity, and the intensity gradient combined with a boundary constraint.

Liang et al. [19] presents a multiscale dynamic programming algorithm, where the approximate vessel wall positions are estimated first in a coarse-scale image, which then guide the detection of the boundaries in fine-scale image. The dynamic programming procedure is used to find a global minimum of the cost function.

The costs are only defined for the posterior media-adventitia interface; the definitions for the anterior and posterior lumen-intima interface are different but of a similar nature. The cost calculations are similar to those presented in the section above, 2.3.2.2, with an extra cost criterion added.

The cost function is composed of the image features, $\tilde{f}_1(p_i)$, $\tilde{f}_2(p_i)$, $\tilde{f}_3(p_i)$, and the geometrical force $g(p_i, p_{i-1})$:

**Boundary smoothness ($g(p_i, p_{i-1})$):** Favors a smoother line. The cost is represented by the square of the finite difference of the distance to a reference line at node $p_i$:

**Intensity gradient ($\tilde{f}_1(p_i)$):** Favors a candidate located at a higher intensity gradient position. The downward intensity gradient, ($grad(p_i)$, is estimated in a 5x5 neighborhood window and normalized. It is the slope at the center of a third-order polynomial surface fitted to the intensity values within the window.

**Brightness below ($\tilde{f}_2(p_i)$):** Favors a candidate immediately above a wide strong echo. The average intensity of $m$ pixels right below $p_i$.

**Darkness above ($\tilde{f}_3(p_i)$):** Favors a candidate immediately below a dark streak. The average intensity of $n$ pixels right above $p_i$ (this is true for finding the media-adventitia boundary, for finding the intima-lumen boundary, this cost criterion would probably favor candidates below a wide hypoechoic area.).

The brightness below and darkness above criteria are similar to a transition criterion in the upward and downward direction.

#### 2.3.2.4 Combination of the intensity gradient and the variance information in intravascular ultrasound video images.

Luo et al. [20] presents a optimization-based detection method for computing the contour of the coronary artery from intravascular ultrasound video images. The method combines the gradient and the variance of the intensity of the image in the radial direction. This method is more robust under high-level noise than methods counting only on the gradient information. The variances of the upper and lower pixels of each point in a given column is summed up as a parameter $S$. The external cost function is composed of the difference of the normalized value of the gradient $G$ and the sum $S$.

$$G(i_j) = I(i+1,j) - I(i,j) \tag{12}$$

$$\begin{aligned} S(i,j) = & \frac{1}{i-1}\sum_{q=1}^{i-1}\left(\left|I(q,j)) - \frac{1}{i-1}\sum_{q=1}^{i-1}(I(p,j))\right|\right)+ \\ & \frac{1}{m-i}\sum_{q=i+1}^{m-1}\left(\left|I(q,j)) - \frac{1}{m-i}\sum_{q=i+1}^{m-1}(I(p,j))\right|\right) \end{aligned} \tag{13}$$

$$C_{ext}(i_j) = S'(i,j) - G'(i,j)) \tag{14}$$

where $i = 1, 2, ....., m-1$ and $j = 1, 2, ....., n$, and $G'$ and $S'$ are the normalized results of $G$ and $S$.

In parallel with Luo deriving this method, Rabben [24] derived the same method for finding the heart wall in cardiac ultrasound. A modified version of this method will be implemented in this thesis.

#### 2.3.2.5 Semi-Automatic method that uses anisotropic edge-preserving smoothing for improved segmentation.

Chan et al. [7] presents a non-linear scheme based on minimization of a variational energy functional that uses all available pixel information for estimating anisotropically smoothed image and edge fields. The method smooths the image field in homogeneous areas, and not i non-homogeneous areas. The resulting edge field allows for robust snake-based vessel contour extraction and IMT measurement.

The anisotropic process for non-linear noise-suppression and edge estimation is performed by jointly estimating a smooth image field, $f$, and corresponding edge field, $s$, which minimize the variational cost function:

$$E(f,s) = \int\int \{ \underbrace{\alpha(1-s)^2 \left\|\nabla_{DS} f\right\|_1}_{SmoothnessConstraint} + \underbrace{\beta \left\|f-g\right\|_1}_{DataFidelity} + \underbrace{\rho/2 \left\|\nabla_{DS} s\right\|_2 + \frac{s^2}{2\rho}}_{EdgeControl} \} dxdy \tag{15}$$

$g$ represents the B-mode image data, $f$ the piecewise constant approximation of $g$, and $s$ is the edge field whose values range between 0 and 1. $\alpha$, $\beta$ and $\rho$ are weighting parameters. $E(f,s)$ describes the smoothing of the image. In areas containing edges, there is no or little smoothing of the image. For every iteration there is smoothing. The smoothness constraint gives high score to jumps in the smoothed field $f$, except in areas containing an edge ($s \approx 1$), moving the smoothing away from edges. The data fidelity term forces $f$ to resemble the original image data $g$. The edge control term adjusts the density of edges in the $s$.

$\nabla_{DS}(\cdot)$ is a directionally sensitive gradient, allowing for user-specified prior edge orientation information;

$$\nabla_{DS}(f) = \zeta(\nabla f \cdot \vec{e}_{\|})\vec{e}_{\|} + (2-\zeta)(\nabla f \cdot \vec{e}_{\perp})\vec{e}_{\perp} \tag{16}$$

$\vec{e}_{\|}$ is a unit vector lying tangentially to the local tissue boundary known a priori to have a particular edge orientation. $\vec{e}_{\perp}$ is a unit vector perpendicular to this direction. The scalar $\zeta$ controls the relative weighting between the perpendicular and parallel components of the intensity gradient.

The cost function $E_{snake}$ is minimized:

$$E_{snake} = \int_0^1 1/2 \left[ a \left\|\vec{x}'(t)\right\|_2^2 + \left\|\vec{x}''(t)\right\|_2^2 \right] - E_{ext}(\vec{x}(t))dt \tag{17}$$

The snake $\vec{x}(t)$ is a deformable curve, $\vec{x} = [x(t), y(t)], t \in [0,1]$. Where $a$ and $b$ control the snake's tension and rigidity respectively, determining the curve's internal cost.

The edge field, $s$, estimated in 15 is used to compute the external cost function.

$$E_{ext}(x,y) = G_{\sigma}(x,y) * s(x,y) \tag{18}$$

where $G_{\sigma}(x,y)$ is a 2D Gaussian with at standard deviation of $\sigma$ which varies the capture range of the active contour. The external cost term pulls the contour toward either the lumen-intima or the media-adventitia boundaries.

This is an advanced and time consuming method. Lately there has been a lot of interest in these partial differential equation image processing methods as they seem very promising. The method is complicated to implement, in this thesis a more simple method for finding the edges will be implemented.

# 3 Materials and methods

This chapter presents the investigations done and methods used. First, a description on acquisition of data and the post processing system. Thereafter, a presentation of the two criteria developed in this thesis, before the feasability study done is described.

## 3.1 Acquisition of data

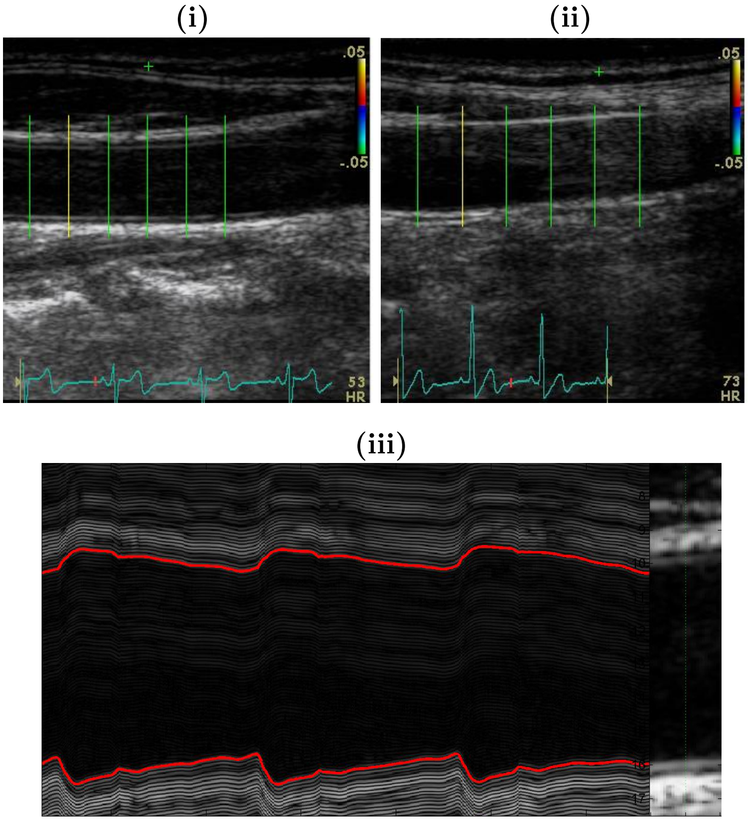

**Figure 14:** Typical images of the Common Carotid, image (i) has visible intima layers, image (ii) has a less visible intima-layer. The green lines represents the ROI selected, where RF data is recorded. (iii) RF m-mode along one beam, on the right hand side of the picture is an extract of the B-mode along the selected beam.

All the datasets were recorded using a Vivid7 scanner, equipped with a 12 MHz linear array transducer, 12L, from GE Vingmed Ultrasound, Horten, Norway. Both B-mode and RF data were recorded; while recording the B-mode, a ROI was selected by the operator, and RF data was recorded along

8 evenly distributed beams within the ROI, with a center frequency of 8MHz for Carotid data and 10MHz for Brachialis data. RF data was stored as IQ demodulated data at a sampling frequency of 10 MHz for both Carotid data and Brachialis data. While recording the TVI data, B-mode imaging was recorded simultaneously. A part of the tissue image was recorded (1/10), then the whole IQ image was scanned, before another 1/10 of of the tissue image was recorded, as explained in section 2.2.3.

To obtain a good contrast between the vessel wall and lumen, the ultrasound beam should be aimed perpendicular to the vessel. Figure 14 shows two typical images of the Common Carotid. Image (i) has a visible intima-layer both along the upper and the lower wall. In image (ii) the intima-layer is only visible for a small section along the lower vessel wall, and there is also more noise in the lumen area. The green lines represents the 8 beams within the ROI where RF data was recorded. Image (iii) shows RF m-mode along one beam with an extract of the B-mode image along the selected beam.

### 3.2 Post processing system/Software system

After the scanning, the raw ultrasound data with separate gray-scale and IQ values were transferred to a personal computer for processing.

GcMat, an internal prototype program, used in research by GE Vingmed and the Department of Circulation and Image Diagnostics at NTNU, makes it possible to view and manipulate ultrasound data recorded by GE Vingmed ultrasound scanners. The program runs under Matlab (The MathWorks Inc., Natick, MA, USA) and consists of two parts:

1. An ActiveX component that reads and displays Vivid7 data.
2. A Matlab toolbox containing the vessel wall detection algorithm.

### 3.3 HUNT fmd-protocol

Flow mediated dilation (FMD) is an endothelium-dependent process that reflects the relaxation of an artery when exposed to increased shear stress. Increased flow, and thereby increased shear stress, through the brachial artery occurs during postocclusive reactive hyperemia. Studies have suggested that the maximal increase in diameter occurs approximately 60 seconds after release of the occlusive cuff. The above is a replica from Corretti et. al [10]. To calculate FMD measurements of the diameter changes are needed. In the HUNT-study, recording like described below are done to measure FMD.

To create a flow stimulus in the brachial artery, a blood pressure cuff is first placed on the upper part of the arm. Then an image is taken when the arm is at a rest state before arterial occlusion is created by cuff inflation for 5 minutes. Subsequent cuff deflation induces a brief high-flow state through the brachial artery to accommodate the dilated resistance vessels. The resulting increase in shear stress causes the brachial artery to dilate. The longitudinal image of the artery is recorded continuously from 30 seconds before to 2 minutes after cuff deflation [10].

After recording the images and the images for analysis are chosen, the boundaries for diameter measurements (either the lumen-intima or the media-adventitia interfaces) are detected manually or automatically. The variability of the diameter measurement is greatest when it is determined from a point-to-point measurement of a single frame, and least when there is an average derived from multiple diameter measurements determined along a segment of the vessel.

## 3.4 Population Study and Limitations

The datasets used in this thesis are taken from three different databases. The 13 datasets used in the parameter tuning while implementing the edge detection criteria are taken form a database containing Carotid recordings from 39 subjects, used in [25]; $\text{Datasets}_{Param}$. 70 datasets with Carotid recordings were provided from the Asklepios study at Gent University Hospital, Belgium [3]; $\text{Datasets}_{Ver}$. These were used in the verification of the two vessel detection methods proposed. Brachialis recordings on one subject were taken according to the HUNT fmd-protocol, see section 3.3, which, together with 4 Brachialis recordings provided from a Master student at Gent University [3], will be used in the Brachialis feasability study; $\text{Datasets}_{Brachialis}$.

The $\text{Datasets}_{Param}$ are recordings of 39 subjects, aged 18-77 with 7 normals and 32 patients. The $\text{Datasets}_{Ver}$ contains 70 datasets, random selected from a large database with more than 2000 Carotid recordings. For all 70 datasets, there is information on vessel diameter in one of the eight beams, that is manually detected in the Asklepios study. Out of these 70 datasets, 22 datasets with visible intima layer were selected and manual tracking of the inner vessel wall was done by two different observers. The manual tracking was done on the same beam as was used in the Asklepios study.

Each dataset in $\text{Datasets}_{Param}$ consists of 3-4 heart cycles. The datasets in

Datasets$_{Ver}$ were 7-10 heart cycles. For memory purposes the datasets were reduced to 3 heart cycles. The quality of the datasets ranges from poor to very good. The aim of the extensions of the algorithm presented here, is to detect the vessel wall edge where there is a visible intima layer. A visible intima layer within the ROI is therefore a criterion for which dataset to use in this thesis.

Only high quality images with visible intima layers have been used in this thesis.

### 3.5 External cost criterion

The existing algorithm, developed by Stein Inge Rabben [23] was in the autumn project extended with a model matching algorithm for scoring candidate points, based on the results from the simulation and studying the signatures [12]. The model chosen was represented by a sum of two Gaussian curves (MMC2). The MMC2 is not robust enough and one of the aims of this thesis was therefore to replace MMC2 with another model matching algorithm. Additionally, a criterion addressing the problem with the transition criterion, by combining the gradient and *std* information, was implemented. The two implemented criteria are presented in this subsection.

#### 3.5.1 GradTrans criterion (GTC)

One of the proposed methods, based on the method derived by Luo [20] and Rabben [24], combines the gradient and standard deviation information in the intensity signature to compute an external cost function. A window of a certain length (WL) is slid over the signature, with the candidate point positioned in the middle of the window. The intensity mean value, $\mu$, and intensity *std*, $\sigma$, is computed for both sides of the candidate point, and the external cost is computed as follows:

$$C_{GTC}(c_i) = (1 - w_{std}) \underbrace{\frac{255 - (\mu_O - \mu_I)}{510}}_{Gradient} + (w_{std}) \underbrace{\frac{w_I * \sigma_I + w_O * \sigma_O}{128}}_{STD} \tag{19}$$

Where I and O denotes inside and outside respectively, and the weighting $w_I$ = (1 - $w_O$). The first part of equation 19 is a gradient operator that favors a leap in average inside and outside of the candidate point. The second part utilizes the *std* information in the intensity signature; it favors flat regions outside and inside of the candidate point. At the edge of the vessel wall, the inside half-window will be positioned in the lumen, where the intensity signature is flat, and hence the $\sigma_I$ is expected to be low. The outside half-window, however, will include parts of the vessel wall, where the intensity signature has high variance. Therefore, the weighting $w_I$ is expected to be much higher than $w_O$. $w_{std}$ is the weighting between the gradient and the STD part of the equation. An illustration of the GTC cost computation can be seen in figure 15.

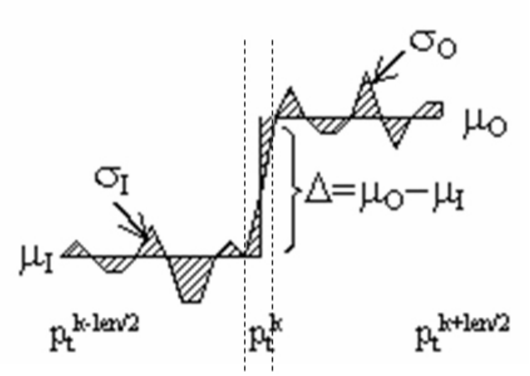

**Figure 15:** Figure illustrating the GTC cost [24].

The middle values of the window, within the dashed lines are disregarded as the leap from dark to bright is not direct, but has a slope that is half a pulse length wide.

To prevent the GTC from scoring and favoring artifacts that can sometimes be seen inside lumen, a constraint was put on. The average intensity in the outside half-window must be of a certain percentage of the maximum intensity ($\%AntAmp$ and $\%PostAmp$ for the anterior and posterior wall respectively), forcing the method to search somewhere close to adventitia, as adventita normally has the highest intensity.

Within the lumen, the variance in intensity is often low. This will be scored positively by the STD part of equation 19. To prevent the STD from overruling the gradient part in areas like this, with low variance, a constraint with a threshold value was put on to score the candidates negatively when within the lumen area.

The various parameters described above was tuned using the ECMT that is described in subsection 3.6. The result of the tuning can be seen in table 1 (see Appendix B.1 for the parameter tuning).

| $WL$ | $w_O$ | $w_{std}$ | $\%AntAmp$ | $\%PostAmp$ |
|---|---|---|---|---|
| $2.079 * 10^{-3} mm$<br>(27 points) | 0 | 0.9 | 40% | 43% |

**Table 1:** An overview of the GTC parameters; , window length (WL), weighting outside (wO), STD weighting (wStd), % amplitude of anterior wall (%AntAmp) and % amplitude of posterior wall (%PostAmp).

#### 3.5.2 Model matching method.

A window is slid over the intensity signature of the chosen beam of the grayscale picture, the parameters of the Gaussian curves are estimated from the data within the windows. Next, the parameters are checked against various criteria to see whether the point meets the qualifications to be an actual candidate. If the parameters do not match the criteria, the point is given a high cost, whereas if the parameters match the criteria, the Gaussian curves are computed and then compared to the actual signature within the window and a score is given to the candidate point.

##### 3.5.2.1 Choosing a model

**Simulation of ultrasound signals**
In the autumn project [12] a simulation in 1D was done to motivate for the model used in the model matching cost criterion.

The 1D simulation was done by making a layer model (figure 16, (ii)) with the various layers in the vessel wall. The lumen, intima, media and adventitia layers were given an acoustic impedance according to tables in [11]. Additionally, as adventitia is a summation of many scatterers at different depths, noise was added to the the adventitia layer. The width of the layers are taken from [28] and [32].

The pulse displayed in figure 16 (i) was used. The resulting received echo plotted in 16 (iii) indicate that there are two main peaks on each side of the lumen, representing the intima-lumen interface and the media-adventitia interface. It is known that the distance between the two peaks is equal to the IMT, a factor that has to be accounted for when making the model; IMT will vary from dataset to dataset.

The received echo in 16 (iii) illustrates the effect the pulse tail has on the vessel wall edges in ultrasound images, as explained in section 2.2.4. The pulse 16 (i) is asymmetric, meaning there is an extension on the trailing side

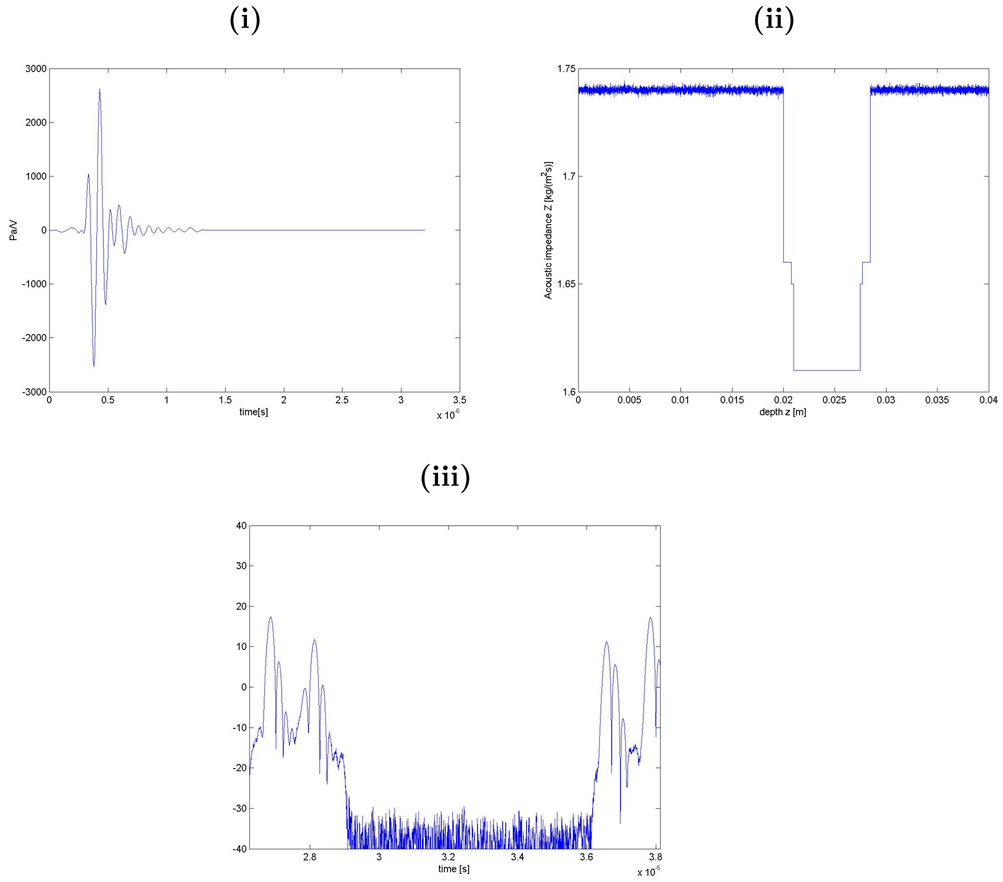

(i)

(ii)

(iii)

**Figure 16:** The pulse (i) and the 1D vessel model with lumen, intima/media and adventitia layers (ii). (iii) plots the envelope of echo signal

of the peak. The extension can be seen in the anterior wall, at the left side of the plot of the received echo the edge between the main lobe and lumen gets smeared out due to the pulse tail. On the right side of the plot, the pulse tail has no effect on the posterior wall edge.

**Intensity signatures across vessel walls**

The intensity signatures from the eight beams of the datasets were, in the autumn project, plotted one by one to see whether what was found in the simulation corresponded with the actual data signatures.

The plotting and studying of the signatures in figure 18 strengthened the observations from the simulation. The smaller peak, corresponding to the intima-lumen interface, is often smooth and has the shape similar to a Gaus-

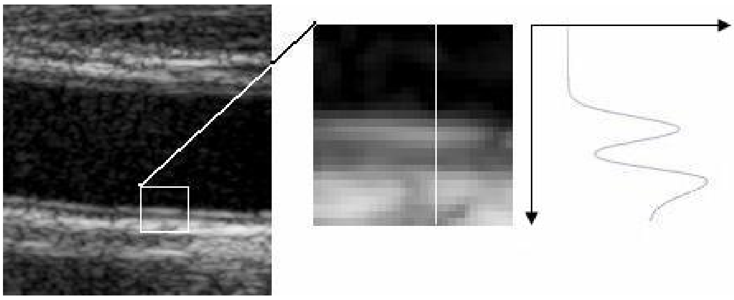

**Figure 17:** Extraction of a signature. This is a modification of figure 5.2 in [14].

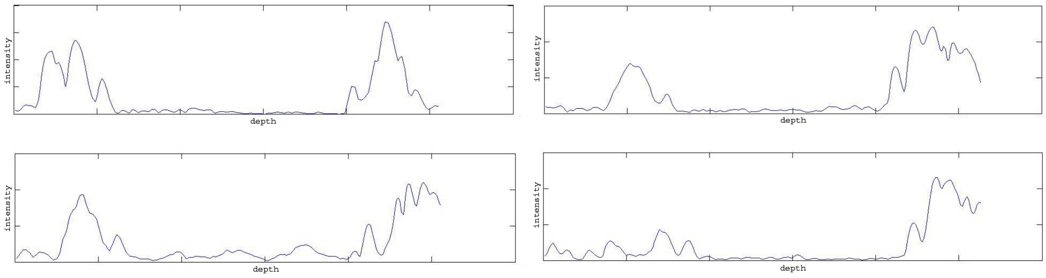

**Figure 18:** A selection of signatures taken from various datasets along beams where there is a visible intima-layer.

sian curve, while the larger peak, corresponding to the media-adventitia interface, is wider, more irregular and bulky. The reason for this is that tunica intima is a single layer of scatters, while tunica adventitia is composed of a set of scatters at different depths, ref. chapter 2.2.4.

From studying both the signatures and the outcome from the simulation indicates that the model should consist of a graph that contains two steps or peaks, one lower than the other. Additionally, the distance between the two peaks or steps has to vary from dataset to dataset. The MMC2 implemented in the autumn project uses two Gaussian curves. A Gaussian curve is not a good representation of adventitia as adventitia is very irregular. However, the slope at the start of the adventitia is often smooth and is related to the pulse length. A half Gaussian curve could therefore be a model for the slope of the adventitia layer. Combining this with a Gaussian curve representing the intima layer, the model presented here is a model consisting of one and a half Gaussian curves.

#### 3.5.2.2 The model matching criterion with 1.5 Gaussian curves (MMC1.5)

The sum of one and a half Gaussian curves model:

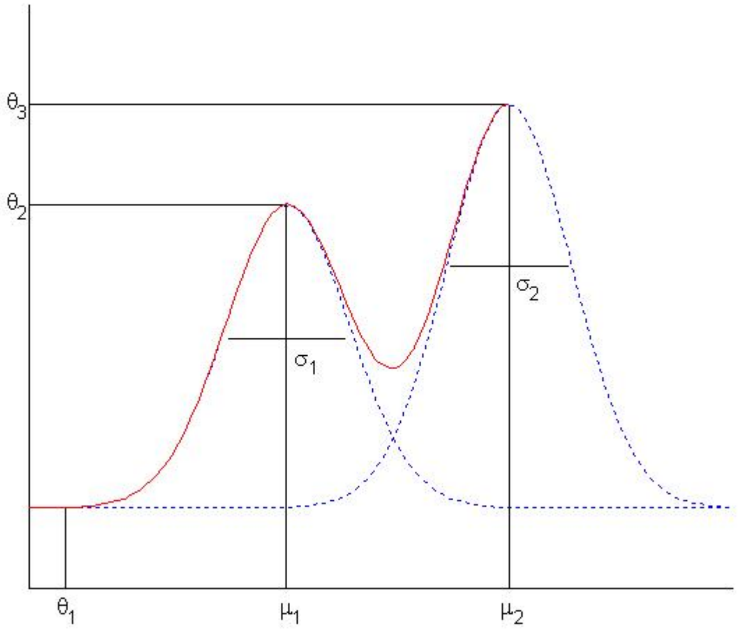

**Figure 19:** Illustration of the model with 1.5 Gaussian curves.

$$f(x) = \theta_1 + (\theta_{int} * e^{-(x-\mu_{int})^2/(2*\sigma_{int})} + \theta_{ad} * e^{-(x-\mu_{ad})^2/(2*\sigma_{ad})}) \tag{20}$$

Where the *int*-parameters represents the intima curve and *ad*-parameters the adventitia curve.

- x represents the row number.
- $\theta_1$ is the offset parameter.
- $\theta_{int}$ and $\theta_{ad}$ are the amplitude parameters for the two Gaussians.
- $\mu_{int}$ and $\mu_{ad}$ are the mean parameters for the two Gaussians.
- $\sigma_{int}$ and $\sigma_{ad}$ are the variance parameters for the two Gaussians.

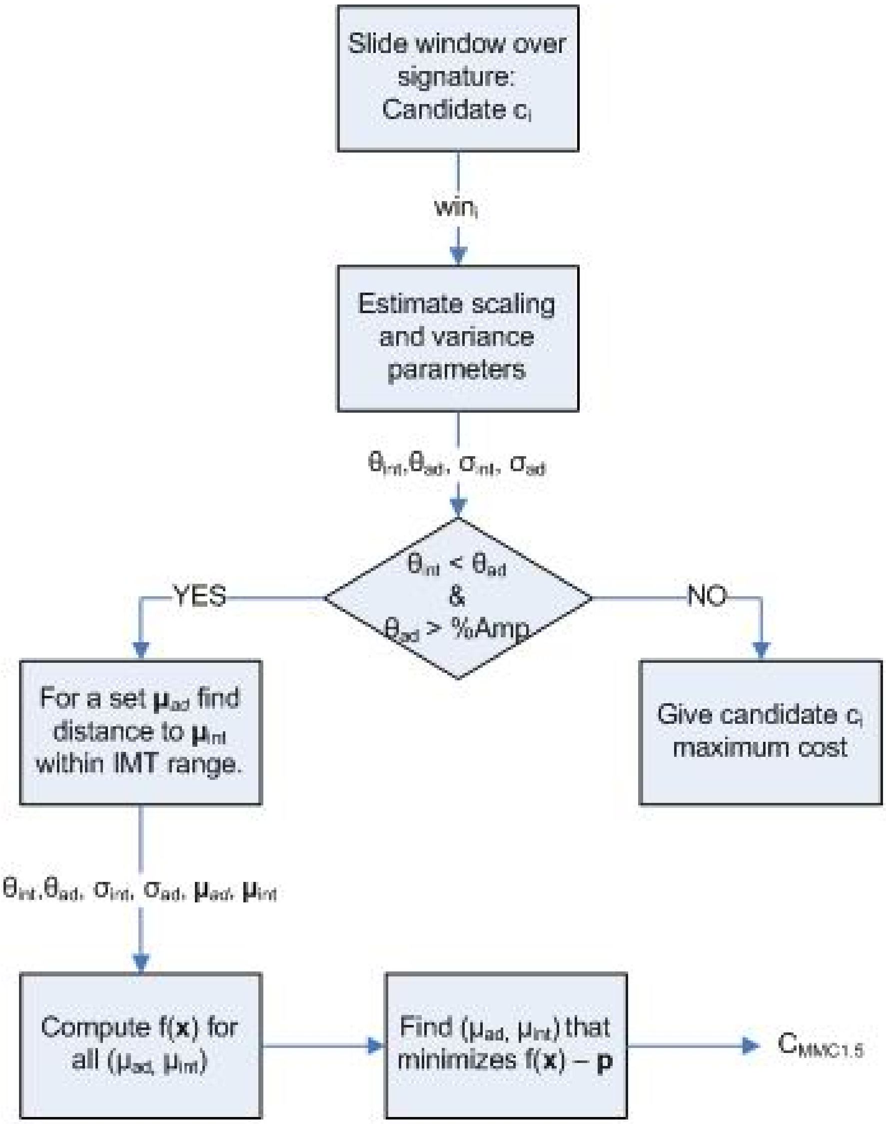

**Figure 20:** Flow chart of the MMC1.5 algorithm.

### Parameter estimation and limiting criteria

$\theta_{int}$ and $\theta_{ad}$ are the scaling parameters, they are given by the maximum value of the intensity signature within the half-window containing the corresponding Gaussian curve. $\sigma_{int}$ represents the width of the intima curve and $\sigma_{ad}$ represents the width of the slope of the adventitia curve. These are given by the pulse length.

As found from the going through the signatures and running the simulation in the autumn project [12], the amplitude of the adventita peak is higher than the amplitude of the intima peak. A criterion using this was implemented; the Gaussian curves were only calculated for $\theta_{ad}$ larger than $\theta_{int}$, for $\theta_{ad}$ smaller than $\theta_{int}$, the candidate was scored maximum cost to make it least attractive.

Inside the ROI, maximum intensity normally lies somewhere within adventitia. The intensity varies for the anterior and posterior adventitia. It is known that the intima-lumen edge lies somewhere near to the adventitia, and hence this can be used as a criterion. The ROI is therefore divided into an anterior and a posterior region, and maximum intensity is found for both. To discard artifacts in the lumen that might correlate with 1.5 Gaussian curves; when $\theta_{ad}$ lower than $\%AntAmp$ and $\%PostAmp$ of the maximum intensity of the anterior and posterior region respectively, the $f(x)$ was not calculated and instead maximum cost was given to the point.

$\mu_{int}$ and $\mu_{ad}$ are the middle positions of the curves representing the intima and the adventitia layer respectively. The distance between $\mu_{int}$ and $\mu_{ad}$ is the intima media thickness (IMT), which is normally between 0.4 and 1.2 mm. When finding the wall, $\mu_{ad}$ is set, and the position for $\mu_{int}$ is found by iterating through the window and testing for the possible and physiological reasonable IMT.

When finding the anterior wall, the candidate point is located at the far right of the window, corresponding to the lumen-intima interface, ref. figure 21. Likewise, when finding the posterior wall, the candidate point is located on the far left of the window.

The final step in the algorithm is to find the sum of the absolute value of the difference between the estimated model and the data. This gives the matching cost.

The cost is illustrated as the beige area in figure 21 and is computed as follows :

$$C_{match}(c_i) = \sum_{j=1}^{n} \left| (\theta_1 + (\theta_{int} * e^{-(j-\mu_{int})^2/(2*\sigma_{int})} + \theta_{ad} * e^{-(j-\mu_{ad})^2/(2*\sigma_{ad})})) - p_j \right| \tag{21}$$

where the parameters $\theta_1$, $\theta_{int}$, $\mu_{int}$, $\sigma_{int}$, $\theta_{ad}$, $\mu_{ad}$ and $\sigma_{ad}$ are calculated as described above, $n$ is the length of the window and $p_j$ is the pixel value in pixel $j$ within the window.

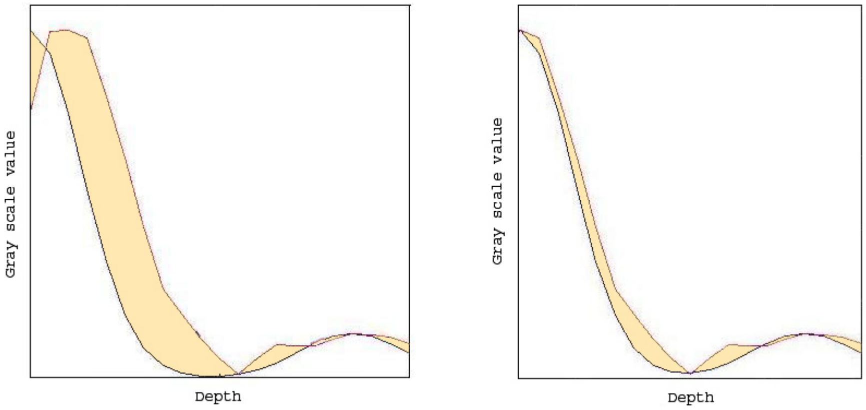

**Figure 21:** Finding the anterior wall, the candidate point is at the very right of the black curve. For each candidate point, the distance between the two curves is changed, to find the best match between signature and estimated curve. Red curve corresponds to the signature and the black curve to the estimated curve. The cost corresponds to the beige area. As the black curve moves further to the right, the area, and hence the cost increases.

The various parameters described above was tuned using the ECMT described in subsection 3.6. The result of the tuning can be seen in the table below. See Appendix B.1 for the parameter tuning.

| $WL$ | $\theta_1$ | $\%AntAmp$ | $\%PostAmp$ |
|---|---|---|---|
| $1.617 * 10^{-3} mm$<br>(21 points ) | $1.001 * 10^{-3} mm$<br>(13 points) | 47% | 45% |

**Table 2:** An overview of the tuning of the MMC1.5 parameters; window length ($WL$), offset value ($\theta_1$), % amplitude of anterior wall ($\%AntAmp$) and % amplitude of posterior wall ($\%PostAmp$).

### 3.6 Edge criteria modeling tool.

An edge criteria modeling tool (ECMT) was made to study how the various external cost criteria score different intensity signatures. Further, the ECMT was used to tune the parameters of the criteria. Intensity signatures were loaded and one signature was selected and displayed at a time. Figure 22 shows an image of the ECMT, where one intensity signature is loaded and MMC1.5 is used. The upper window of the figure plots the signature, the middle window plots the bright-to-dark cost (red) on the signature (blue) and the lower window plots the dark-to-bright cost (red) on the signature (blue) (finding the posterior wall). The lower the cost, the better the candidate point.

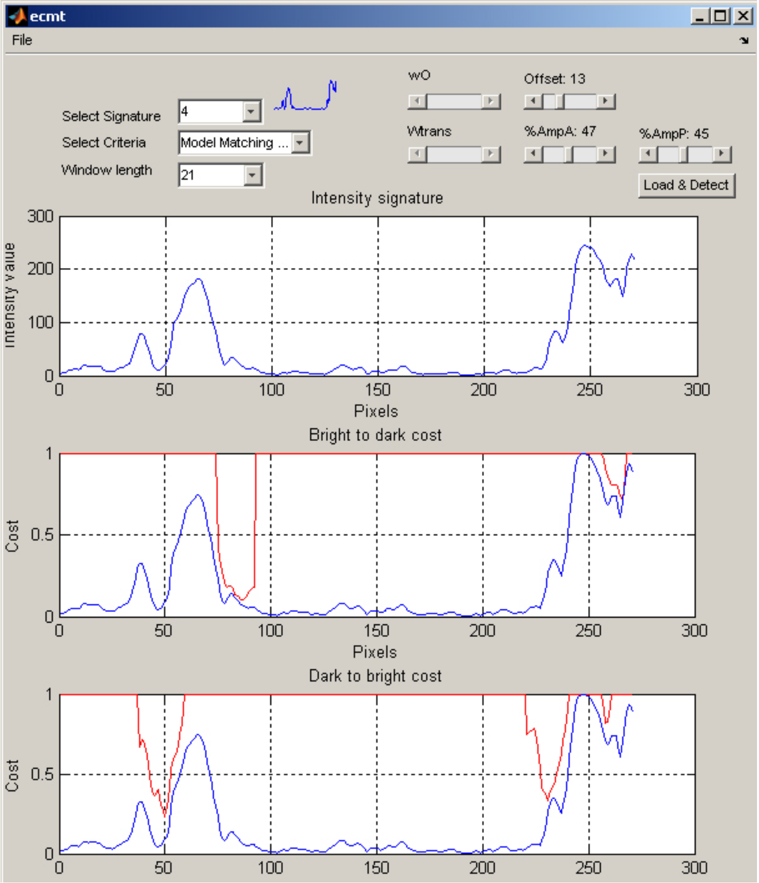
ecmt

Select Signature: 4

Select Criteria: Model Matching ...

Window length: 21

Offset: 13

%AmpA: 47

%AmpP: 45

**Figure 22:** Edge criteria modeling tool.

Datasets$_{param}$, table 7 in Appendix B.1, were used in the parameter tuning. Two beams with visible intimalayer were selected from each dataset. The parameters described in the previous sections, seen in the upper right hand side of figure 22, were tuned for GTC and MMC1.5. The result of the tuning can be seen in Appendix B.1, tables 8 and 9.

## 3.7 Feasability study on Brachialis wall detection.

A feasability study to see whether the AVDA application can improve the efficiency of the Flow Mediated Dilation (FMD) analysis, by automatically detecting the Brachialis vessel wall and calculating the inner diameter will be done. As the Brachialis vessel is smaller than the Carotid vessel, the intima layer is most often not visible in the ultrasound images of the vessel. Testing the various cost criteria, both existing and those presented in this thesis, will be done to find which criterion is best for detecting the vessel wall in Brachialis recordings.

A recording according to the HUNT fmd-protocol, see section 3.3, will be taken, to see whether the diameter change in Brachialis can be measured using the AVDA.

## 3.8 Verification and comparison of the various methods.

A code to manually select and save the edge points in a trigger point in the RF image was implemented.

On 22 datasets from Datasets$_{Ver}$ manual measurement of the intima-lumen boundary was done by two different observers. The aim of this was to do a reproducibility study between the two observers. In addition, these datasets were used in the verification of the two implemented cost criteria, GTC and MMC1.5, by comparing the automatically detected edges with manually measured vessel wall.

The information on manually tracked inner-diameter done by one observer in the Asklepios study [3] in Datasets$_{Ver}$ was used to compare automatically with manually estimated inner-diameter. This was done on 49 of the 70 datasets in Datasets$_{Ver}$.

The datasets in Datasets$_{Brachialis}$ were used in the Brachialis feasability study.

# 4 Results

This chapter presents the results achieved in the thesis. First, a visual presentation of the results of the two edge detection criteria implemented, thereafter the results of the verification of the two criteria. Finally, the results achieved in the feasability study on the brachial artery wall detection is presented.

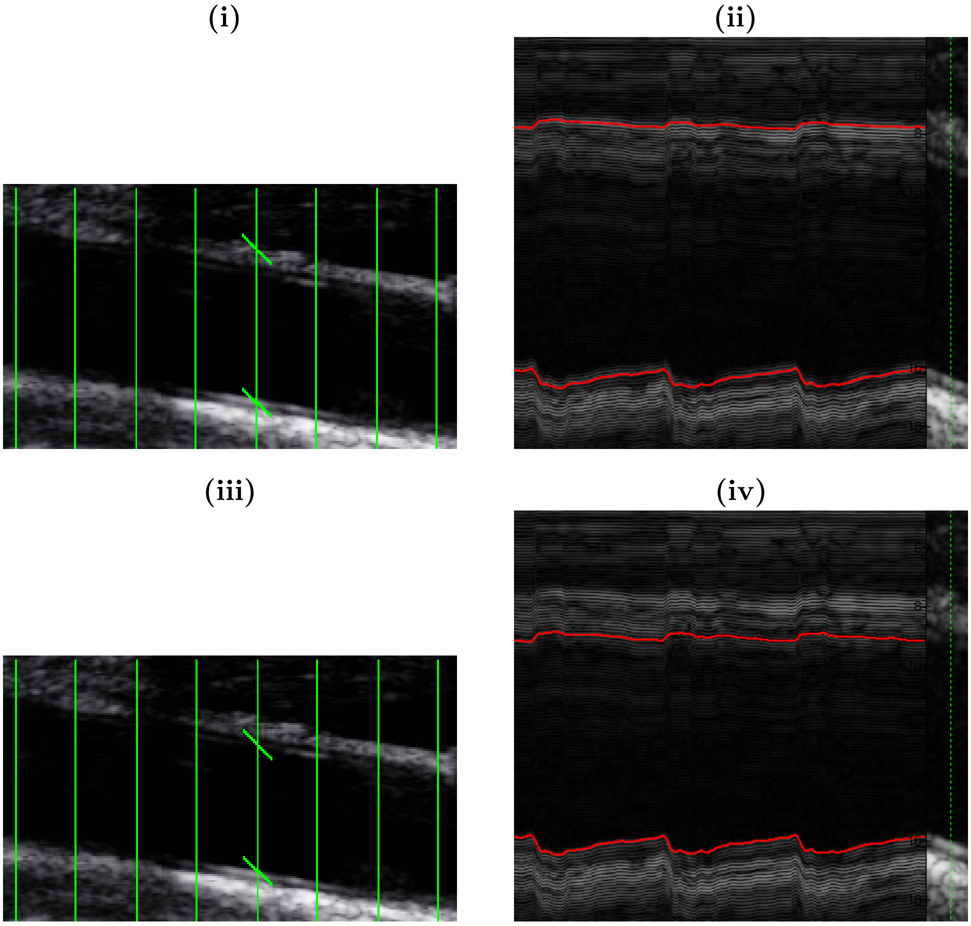

**Figure 23:** Carotid vessel wall detection in beam number 5, dataset number 18, using the GTC criterion (i) and MMC1.5 (iii). RF image of beam number 5 showing the wall detection using the GTC criterion (ii) and MMC15 (iv).

## 4.1 Edge detection - Carotid

Figure 23 and 24 shows the result of using GTC criterion, (i) and (ii), versus MMC1.5 criterion, (iii) and (iv), when detecting the Carotid vessel intima-lumen boundary. The detected edge is the crossing of the beam and the oblique line. The RF images shows the selected beam through the heart cycles, with the detected edges plotted.

Figure 25 visually presents the results of the GTC and MMC1.5 criterion on a selection of the datasets. The images show that the MMC1.5 criterion seems to detect the correct vessel wall in many of the images, whereas the GTC criterion fails more often. In dataset number 5, the MMC1.5 fails completely and detects the anterior wall to be at a structure within the wall. In dataset 16, an artifact in the lumen is detected by the MMC1.5. The result on the remaining datasets can be seen in Appendix C.2.

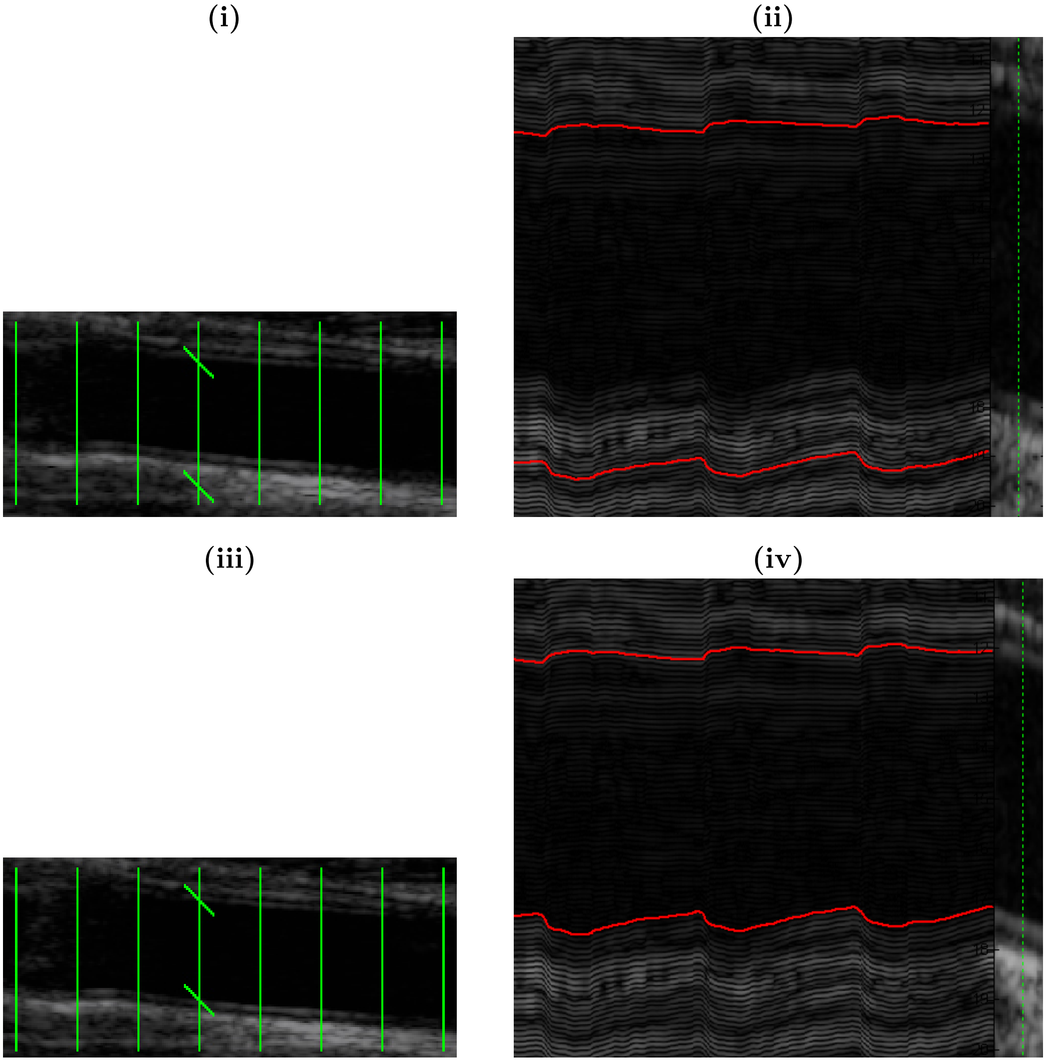

**Figure 24:** Carotid vessel wall detection in beam number 5, dataset number 4, using the GTC criterion (i) and MMC1.5 (iii). RF image of beam number 5 showing the wall detection using the GTC criterion (ii) and MMC15 (iv).

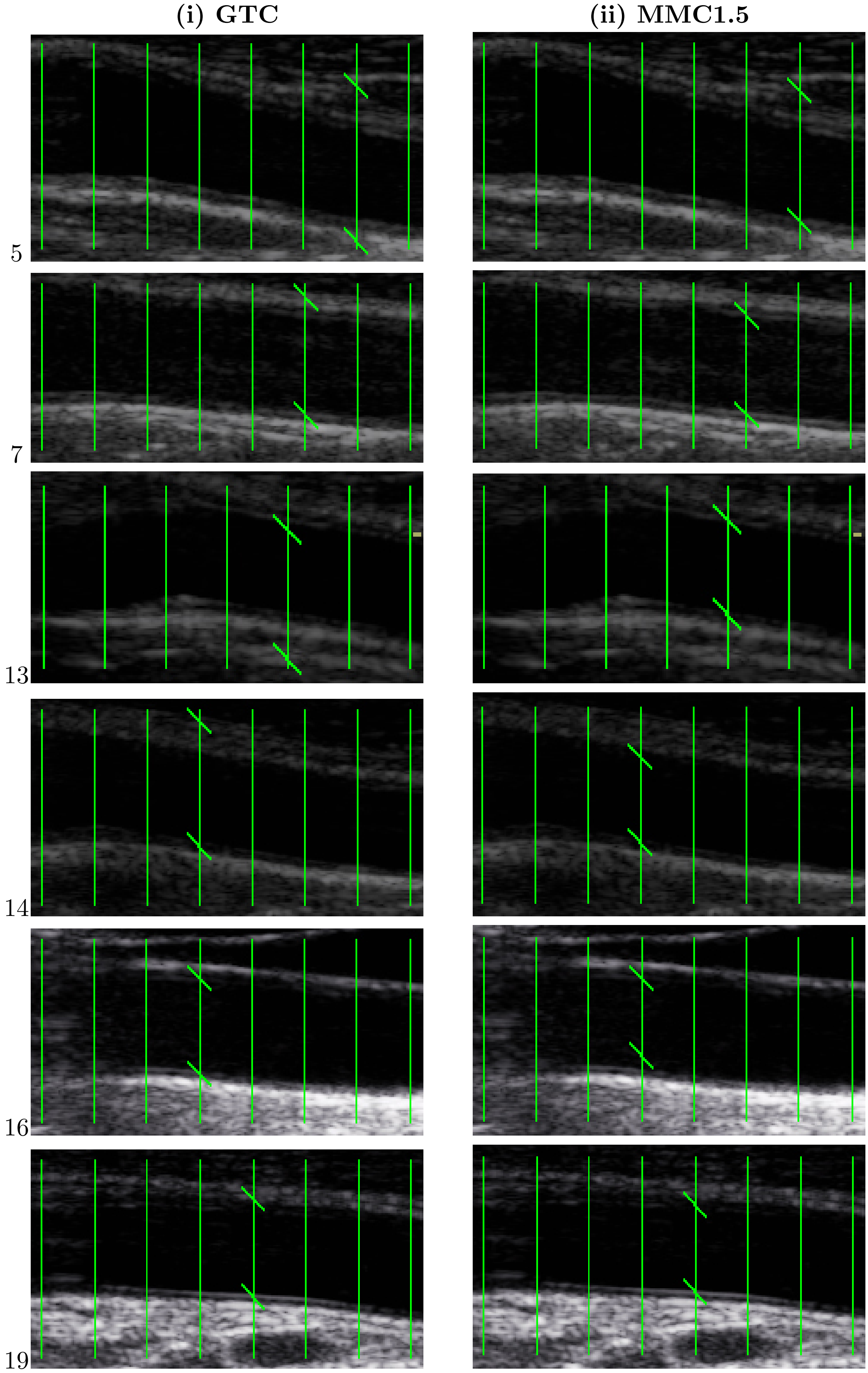

**Figure 25:** Visual Carotid wall detection of datasets 5, 7, 13, 14, 16 and 19 using both GTC (i) and MMC1.5 (ii) criterion.

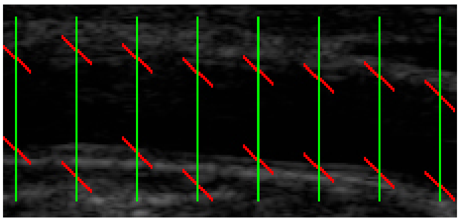

**Figure 26:** Dataset 12; MMC1.5 detection on all eight beams (beam number 4 is the selected beam).

Figure 26 show MMC1.5 detection on all eight beams, illustrating that the detection works on some of the beams and fails on other. The detection on the selected beam (beam number 4) fails, while it works on the neighboring beams.

## 4.2 Verification of edge detection criteria

The following subsections presents the result of the verification of the GTC and MMC1.5 criteria.

### 4.2.1 Verification using manual detected edges

In the 22 provided datasets (from $\text{Datasets}_{ver}$) presented in Appendix C.1, table 10, manual detection of the Carotid intima-lumen interface in the anterior and posterior wall was done by two different observers. Figure 27 presents histograms of the difference in detection by the two observers. The upper histogram shows the difference in detection of the anterior wall, with the inter-observer difference having $\mu_a = -0.087\text{mm}$ and $\sigma_a = 0.180\text{mm}$. The inter-observer difference in detection of the posterior wall, represented by the middle histogram, is a bit lower and has $\mu_p = -0.045\text{mm}$ and $\sigma_p = 0.164\text{mm}$. The lower histogram shows the diameter difference, $\mu_d = 0.041\text{mm}$ and $\sigma_d = 0.104\text{mm}$.

Table 3 and 4 presents the result of the verification of GTC and MMC1.5 respectively. The three first colons show the difference, in detected anterior wall, posterior wall and diameter, between using the selected criterion and using manual detection (GTC/MMC1.5 - manual). The colon at the far right show the difference in diameter divided by manually detected diameter, presented in %. The manual detection reference is the average of the detection done by the two observers described above.

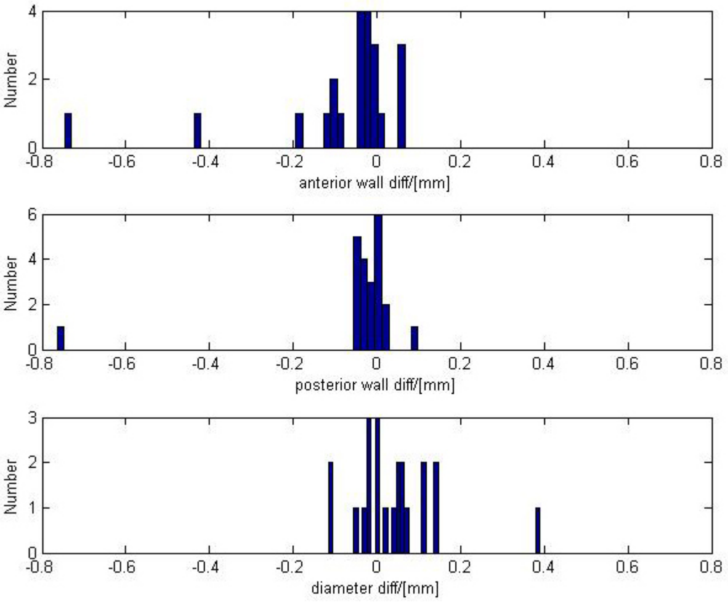

**Figure 27:** Histograms showing inter-observer difference in detection of the anterior wall (upper histogram), posterior wall (middle histogram) and diameter (lower histogram).

Figure 28 presents the resulting histograms of the detection differences, comparing the two automatic detection criteria with manual detection. The histograms in (i) show that GTC detects both the anterior and posterior wall to be within the wall, resulting in an overestimated inner diameter. The MMC1.5 histograms (ii) shows that this criterion detects the edges more correct than the GTC, with some outlays that were detected completely incorrect. The MMC1.5 diameter bias is 7.4% when relating the error to actual vessel diameter, compared with a diameter bias of 30.4% by GTC. For both criteria, the posterior walls are detected more correctly than the posterior walls. The mean and *std* of the histograms in figure 28 are presented in table 3 and 4.

When the detection fails completely and this is clearly seen in the image, an operator would probably discard the detection on that beam. Based on this assumption, the datasets where the MMC1.5 detection fails completely were removed to be able to study the result on the datasets where the detection did not completely fail. For MMC1.5 in figure 28 (ii), the histograms showing the anterior and posterior wall, the datasets where the difference between manual detection and the MMC1.5 detection were larger than 1 mm were removed (outside the red section). For the diameter difference histogram, the datasets where the detection on either the anterior or the

| Dataset | Ant wall diff [mm] | Post wall diff [mm] | Diam diff [mm] | Diam diff/ Manual diam [%] |
|---|---|---|---|---|
| 1 | -1.553 | 0.585 | 2.138 | 39.5 |
| 2 | -0.806 | 1.601 | 2.407 | 44.7 |
| 3 | -0.608 | 0.639 | 1.247 | 18.5 |
| 4 | -1.732 | 0.341 | 2.073 | 40.9 |
| 5 | -3.059 | 1.283 | 4.342 | 76.0 |
| 6 | -0.689 | 0.347 | 1.035 | 22.2 |
| 7 | -1.112 | 0.499 | 1.610 | 27.4 |
| 8 | -0.929 | 0.392 | 1.321 | 23.6 |
| 9 | -1.084 | 0.016 | 1.100 | 18.7 |
| 10 | -0.640 | 0.005 | 0.645 | 13.2 |
| 11 | -0.505 | 2.201 | 2.706 | 63.4 |
| 12 | 0.151 | 0.527 | 0.375 | 7.5 |
| 13 | 0.230 | 2.530 | 2.300 | 46.4 |
| 14 | -2.664 | 0.325 | 2.989 | 59.7 |
| 15 | -0.451 | 0.382 | 0.833 | 13.7 |
| 16 | -0.309 | 0.140 | 0.449 | 08.1 |
| 17 | -1.107 | 0.456 | 1.562 | 27.3 |
| 18 | -1.673 | 0.015 | 1.688 | 26.9 |
| 19 | -0.984 | 0.012 | 0.996 | 18.2 |
| 20 | -0.883 | -0.009 | 0.874 | 14.4 |
| 21 | -2.377 | 0.374 | 2.751 | 43.1 |
| 22 | -0.935 | 0.042 | 0.977 | 15.6 |
| $\mu$ | 1.078 | -0.577 | 1.655 | 30.4 |
| $\sigma$ | 0.828 | 0.704 | 0.975 | 18.9 |

**Table 3:** Table displaying the difference in automatic detection GTC and manual detection (GTC - manual) for the anterior and posterior wall, and diameter difference. The right column displays the diameter difference over manually detected diameter (in %). The $*$ indicates that the dataset is an outlay and is removed in the calculation of $\mu*$ and $\sigma*$

posterior wall failed were removed. Two datasets were removed from the anterior wall detection, tree from the posterior wall detection, resulting in five datasets being removed from the diameter detection. These datasets are indicated with a star, ($*$), in table 4.

Figure 29 shows conventional scatter plots to compare manual detection with the automatic methods. The points in the MMC1.5 scatter plots lie closer to the equality-diagonal than the points in the GTC scatterplots. In the GTC vessel diameter scatter plot, all the points lie above the equality-diameter.

| Dataset | Ant wall diff [mm] | Post wall diff [mm] | Diam diff [mm] | Diam diff/ Manual diam [%] |
|---|---|---|---|---|
| 1 | -0.530 | 0.263 | 0.794 | 14.6 |
| 2 | -0.101 | 0.295 | 0.395 | 7.3 |
| 3 | -0.398 | 0.419 | 0.817 | 12.1 |
| 4 | -0.471 | 0.0134 | 0.485 | 9.6 |
| 5 | -2.706 * | -0.055 | 2.651 * | 46.4 * |
| 6 | -0.292 | 0.115 | 0.406 | 8.7 |
| 7 | 0.083 | 0.499 | 0.415 | 7.1 |
| 8 | -0.480 | 0.058 | 0.538 | 9.6 |
| 9 | -0.572 | -0.104 | 0.468 | 7.9 |
| 10 | -0.342 | -0.148 | 0.194 | 4.0 |
| 11 | -0.577 | 0.023 | 0.600 | 14.1 |
| 12 | 0.333 | 1.670 * | 1.336 * | 26.6 * |
| 13 | -0.250 | -0.011 | 0.239 | 4.8 |
| 14 | -0.204 | -0.037 | 0.167 | 3.3 |
| 15 | -0.118 | -1.122 * | -1.004 * | -16.6 * |
| 16 | -0.187 | -1.264 * | -1.076 * | -19.4 * |
| 17 | -0.290 | -0.633 | -0.344 | -6.0 |
| 18 | -0.409 | 0.015 | 0.424 | 6.7 |
| 19 | -0.334 | -0.066 | 0.268 | 4.9 |
| 20 | -1.306 * | -0.099 | 1.206 * | 19.8 * |
| 21 | -0.161 | -0.055 | 0.106 | 1.7 |
| 22 | -0.324 | -0.681 | -0.357 | -5.7 |
| $\mu$ | -0.438 | -0.041 | 0.397 | 7.4 |
| $\mu*$ | -0.281 | -0.010 | 0.330 | 6.2 |
| $\sigma$ | 0.591 | 0.582 | 0.771 | 13.6 |
| $\sigma*$ | 0.223 | 0.290 | 0.323 | 5.8 |

**Table 4:** Table displaying the difference in automatic detection MMC1.5 and manual detection (MMC1.5 - manual) for the anterior and posterior wall, and diameter difference. The right column displays the diameter difference over manually detected diameter (in %). The $*$ indicates that the dataset is an outlay and is removed in the calculation of $\mu*$ and $\sigma*$.

**(i) GTC**

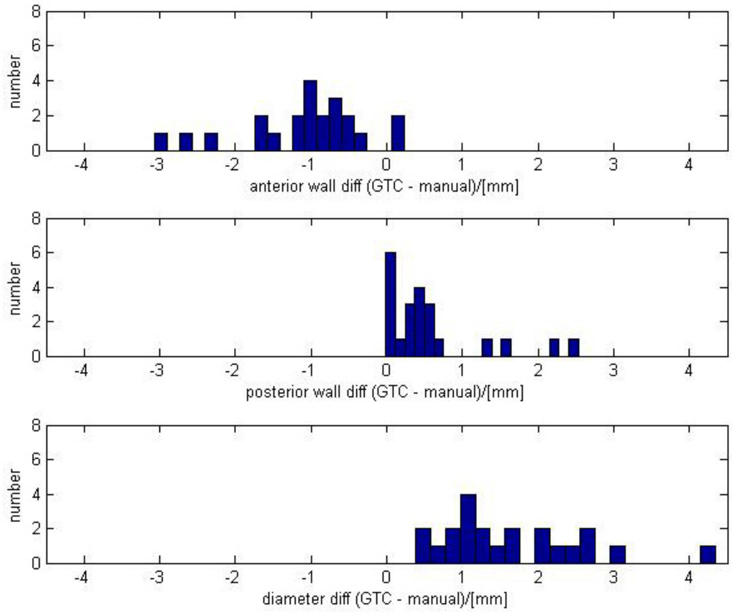

**(ii) MMC1.5**

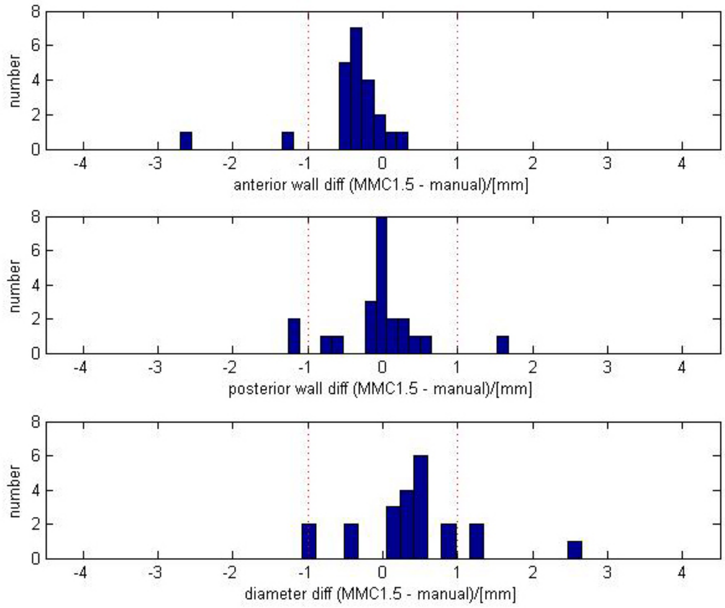

**Figure 28:** Differences between GTC vs manual detection (GTC - manual) (i) and MMC1.5 vs manual detection (MMC1.5 - manual) (ii) in anterior wall (upper histograms), posterior wall (middle histograms) and diameter (lower histograms). The datasets outside the dotted red lines are the datasets that fail completely in MMC1.5, indicated with a $*$ in table 4.

**(i) GTC**

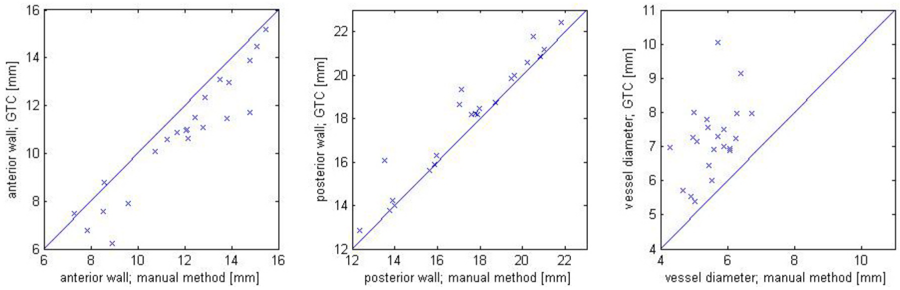

**(ii) MMC1.5**

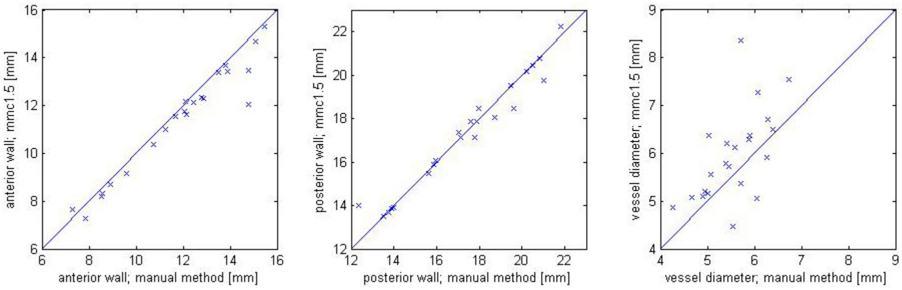

**Figure 29:** Plotting manual detection against automatic detection using GTC, (i), and MMC1.5, (ii) of the anterior wall, posterior wall and diameter.

### 4.2.2 Verification using manual measured diameter

For 49 random selected datasets out of the 70 provided in Datasets$_{Ver}$, AVDA using GTC and MMC1.5 was used to estimate the vessel diameter in one selected beam at four ecg trigger points. This was then compared with the diameter manually detected in the same beam at the four ecg trigger points. Figure 30 presents histograms of the detection error (GTC/MMC1.5 - manual) for the 49 datasets at the four ecg trigger points (upper histograms) and averaged over the trigger points (lower histograms). The mean value, $\mu_{diamDiff}$, and *std*, $\sigma_{diamDiff}$, for the detection error of the two criteria are given in table 5. In addition, the mean value, $\mu_{\%-diamDiff}$, and *std*, $\sigma_{\%-diamDiff}$, of the diameter differences divided by manual detected diameter are shown to relate the error to the actual vessel diameter. After removing the outlays, where the diameter detection error was more than 1 mm (the 12 datasets outside the red dotted lines in figure 30), $\mu^*_{diamDiff}$ increased to 0.146 mm and $\sigma^*_{diamDiff}$ reduced to 0.347.

| | Criterion | n | $\mu_{diamDiff}$ | $\sigma_{diamDiff}$ | $\mu_{\%-diamDiff}$ | $\sigma_{\%-diamDiff}$ |
|---|---|---|---|---|---|---|
| Diameter | GTC | 49 | 1.237 | 1.211 | 21.5% | 20.9% |
| | MMC15 | 49 | 0.014 | 1.056 | 1.3% | 15.7% |

**Table 5:** Mean value, $\mu_{diamDiff}$, and and *std*, $\sigma_{diamDiff}$, of the diameter differences between manual and automatic detection. $\mu_{\%-diamDiff}$ and $\sigma_{\%-diamDiff}$ is the average and *std* of the diameter differences divided by manual detected diameter in %.

Figure 31 and 32 presents Bland-Altman plots [5] of the error in the detection of the Carotid vessel diameter using GTC and MMC1.5 respectively, together with the conventional scatter plots. In nearly all the datasets the diameter detected by GTC is overestimated as most points lie above the equality-diagonal in the scatter plots. In the MMC1.5 scatter plots however, the points lie closer to the diagonal The mean in the MMC1.5 Bland-Altman plot is 0.014 mm compared to 1.237 mm in the GTC Bland-Altman plot, see table 5.

**(i) GTC**

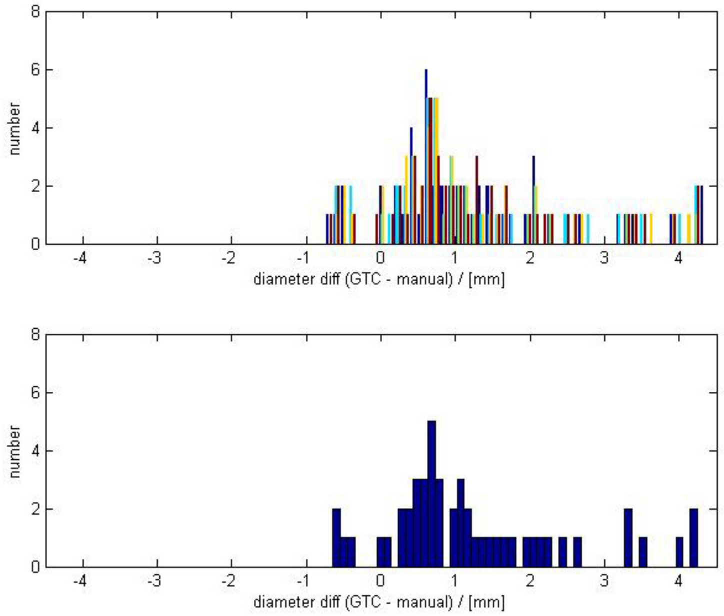

**(ii) MMC1.5**

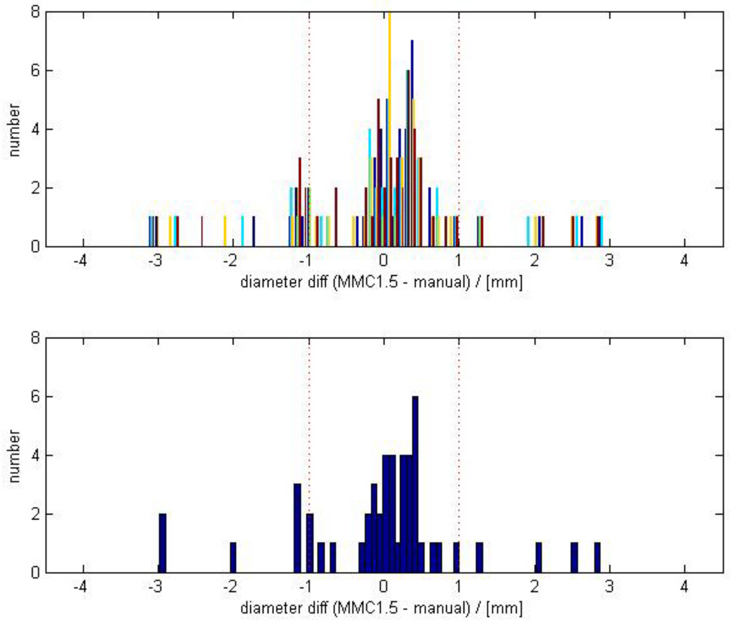

**Figure 30:** Upper histograms in showing differences between manual vs GTC (i) and manual vs MMC1.5 (ii) in diameter measurement at four different ecg trigger points (GTC/MMC1.5 - manual). Lower histograms showing differences between manual vs GTC (i) / MMC1.5 (ii) in diameter measurement, averaged over the four ecg trigger points.

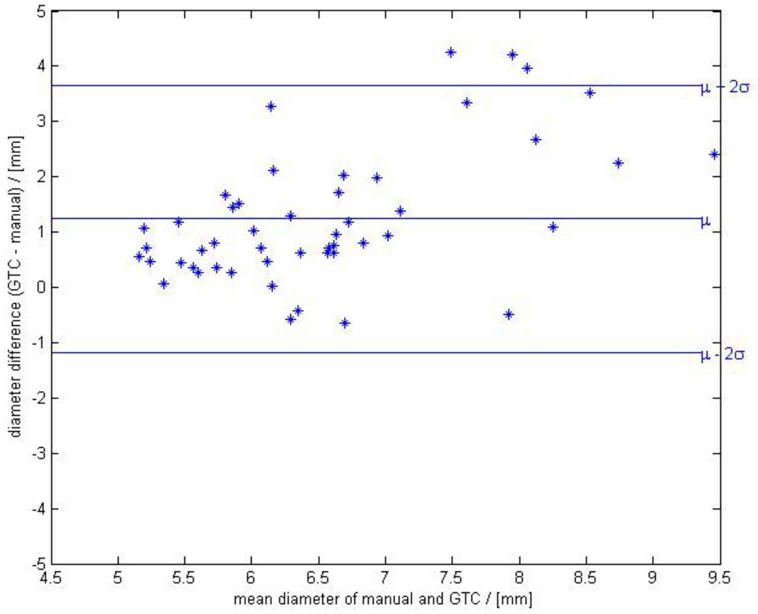

(i) GTC

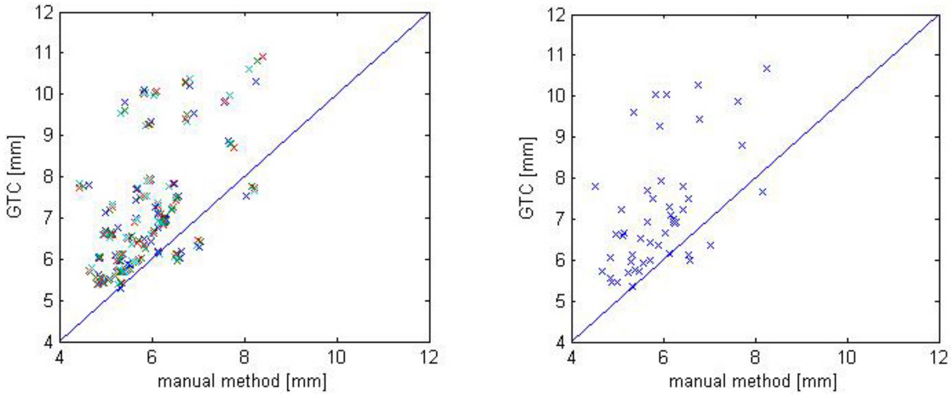

(ii) manual vs GTC

(iii) manual vs GTC

**Figure 31:** Bland-Altman plot and conventional scatter plots of the difference between manual detection and automatic detection using GTC. (ii) show plots the manual detected diameter in 4 ecg trigger points against automatic detected diameter in the same trigger points, while (iii) shows the diameters averaged over the 4 ecg trigger points.

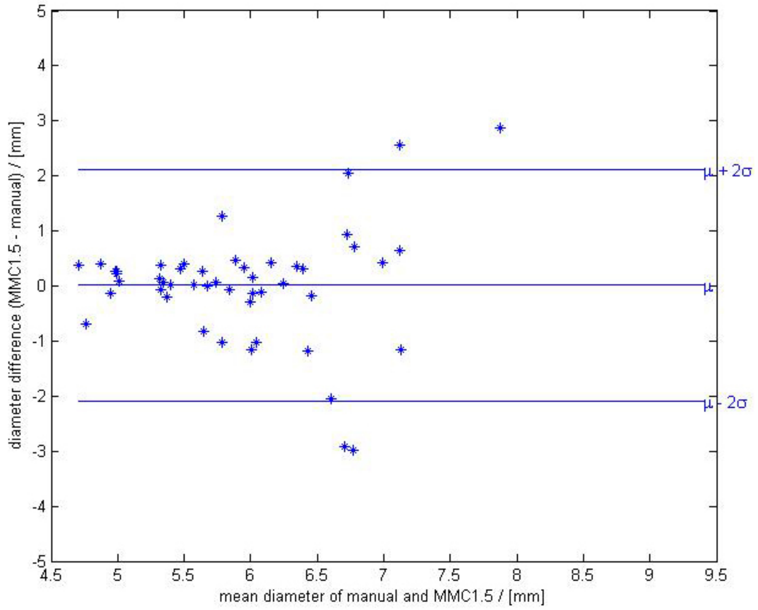
(i) MMC1.5

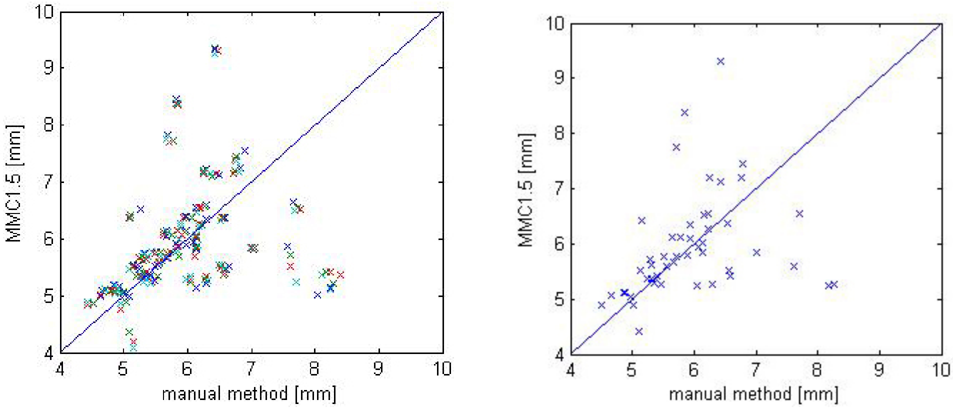
(ii) manual vs MMC1.5

(iii) manual vs MMC1.5

**Figure 32:** Bland-Altman plot and conventional scatter plots of the difference between manual detection and automatic detection using GTC. (ii) show plots the manual detected diameter in 4 ecg trigger points against automatic detected diameter in the same trigger points, while (iii) shows the diameters averaged over the 4 ecg trigger points.

### 4.2.3 Computation time

The Profiler in Matlab was used to record the computation time of the various algorithms. The testing was done on a 1.40GHz Pentium M processor. The times are displayed in table 6. The improvement on MMC2 has decreased the computation time (MMC2$_{new}$ vs MMC2$_{old}$). The MMC2$_{new}$ and MMC1.5 computation time is still high compared to the computation time of the other criteria.

| Filename | HC | Gradient [sec] | Transition [sec] | MMC2$_{old}$ [sec] | MMC2$_{new}$ [sec] | GTC [sec] | MMC1.5 [sec] |
|---|---|---|---|---|---|---|---|
| rv1 | 3 | 0.88 | 1.00 | 70.37 | 26.87 | 0.74 | 20.68 |
| da2 | 3 | 0.57 | 0.71 | 48.70 | 17.83 | 0.50 | 13.53 |
| dh1 | 3 | 0.60 | 0.83 | 50.76 | 20.69 | 0.48 | 15.30 |
| pd1 | 3 | 0.53 | 0.69 | 47.70 | 19.03 | 0.59 | 13.01 |
| mv1 | 4 | 1.52 | 1.45 | 89.37 | 35.20 | 0.97 | 24.14 |
| mt1 | 3 | 0.75 | 1.02 | 62.73 | 24.96 | 0.77 | 17.91 |
| ds1 | 3 | 0.61 | 0.81 | 53.49 | 19.69 | 0.56 | 14.85 |
| dsj1 | 3 | 0.90 | 1.22 | 80.40 | 29.79 | 0.88 | 26.28 |
| vt1 | 3 | 0.73 | 0.95 | 65.59 | 25.34 | 0.78 | 18.41 |
| bl1 | 3 | 0.68 | 0.95 | 60.78 | 24.61 | 0.66 | 18.53 |
| vvl1 | 3 | 0.62 | 0.90 | 52.83 | 20.36 | 0.58 | 14.26 |

**Table 6:** The time consumption of the various criteria for the datasets tested on in the autumn project, containing 3-4 heart cycles (HC).

## 4.3 Feasability study - Brachialis wall detection.

The various criteria implemented in the autumn project (MMC2), in this thesis (GTC and MMC1.5), and the already existing criteria (Transition and Gradient) were tested on ultrasound images of the Brachialis artery to see whether the edges can be detected using the AVDA and hence improve the efficiency of the FMD analysis. Figure 33 and 34 show the result of the automatic wall detection with the various criteria. The results on more datasets can be seen in Appendix C.3. The Gradient criterion seems to give the best result in these images.

In figure 35, the detected Brachialis artery walls and accompanying estimated diameters using the Gradient criterion are shown. The images are taken according to the HUNT fmd-protocol. Image (i) is taken before putting on the cuff, image (ii) is taken approximately 30 seconds after the release, image (iii) approximately 60 seconds after the release and image (iv) 2.5 minutes after releasing the cuff.

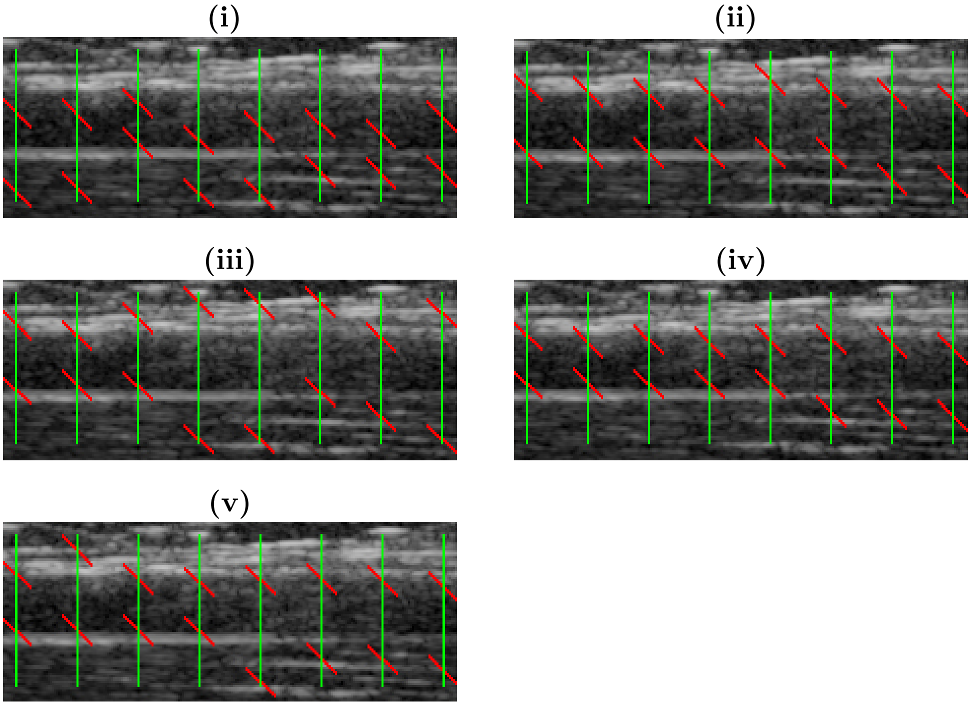

**Figure 33:** Detecting the Brachialis vessel wall using the various external cost criteria: Transition (i), Gradient (ii), GTC (iii), MMC1.5 (iv) and MMC2 (v).

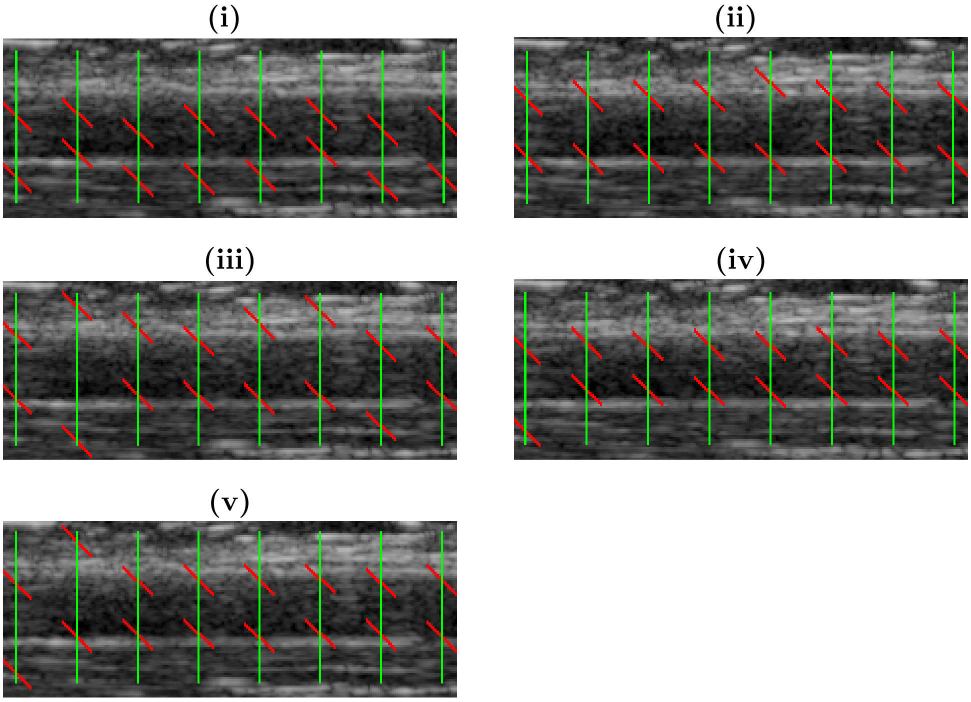

**Figure 34:** Detecting the Brachialis vessel wall using the various external cost criteria: Transition (i), Gradient (ii), GTC (iii), MMC1.5 (iv) and MMC2 (v).

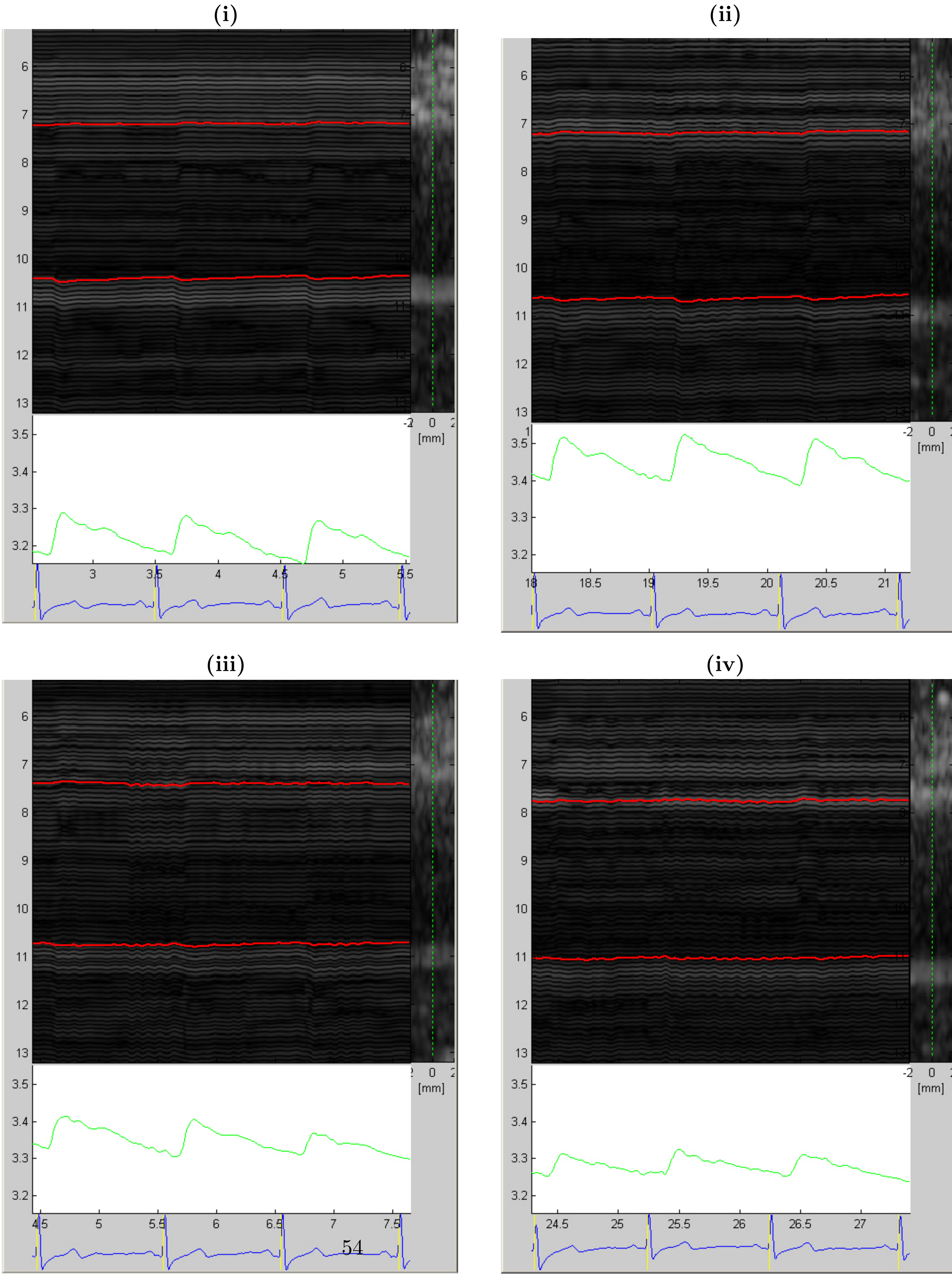
(i)
(ii)
(iii)
(iv)

**Figure 35:** RF image and accompanying detected diameter in beam number 4 using the Gradient criterion in images taken according to the HUNT fmd-protocol, see section 3.3, (i) before putting on the cuff, (ii) 30 sec after release, (iii) 60 sec after release and (iv) 2.5 min after release.

# 5 Discussion

In this chapter there will be an evaluation of the results presented in the previous chapter.

## 5.1 Edge detection

In this subsection there will first be an evaluation on the interobserver results, before the aspects of the two implemented edge detection criteria are discussed. Finally, there will be a discussion on the common issues concerning both the GTC and MMC1.5 algorithms.

### 5.1.1 Interobserver

Manual detection of the intima-lumen boundary was done by two different observers allowing for studies on interobserver differences. Figure 27 indicates that the posterior wall is the easier wall to detect, whilst finding the anterior wall is more complex; the variance between the two observers is greater in the anterior wall than in the posterior wall. The reason for this is probably because in most images the posterior wall has a sharper edge than the anterior wall. This is due to the pulse tail that causes the intima-lumen boundary in the anterior wall to be affected by the echoes from adventitia, see section 2.2.4. The higher variance in interobservability in manually detection of the anterior wall alludes that automatically detecting the anterior wall will also be more difficult than detecting the posterior wall.

As seen from above, using the manual detected points as a golden standard is necessarily not correct, something that has to be taken into account when evaluating the automatic detection algorithms.

### 5.1.2 GTC algorithm

The images presented in the results section 4.1, figures 23, 24 and 25, indicates that the algorithm is not a very good criterion for detecting the intima-lumen interface. In datasets 5 the GTC algorithm fail completely to detect both the anterior and posterior wall, whereas for the other datasets the criterion approximately detects either the anterior or the posterior wall. The images in the results chapter and in appendix C.2 shows that the criterion often incorrectly detects the edge to be at the media-adventitia transition instead of the intima-lumen transition.

All three histogram in figure 28 (i) have a bias, and are asymmetric around the bias. Studying the histograms shows that the anterior intima-lumen interface is detected to be somewhere within the wall in all but two datasets, the mean value of the detection error when comparing to manual detection is 1.078 mm and the *std* is 0.828 mm. For the posterior wall, however, the detection seems better, in some of the datasets the edge is detected correctly, and in the rest, the edge is detected to be somewhere within the wall (bias is -0.577 mm and *std* is 0.704 mm). As in most incidents both the anterior and posterior wall are detected to be within the vessel wall, the vessel diameter is overestimated by using the GTC algorithm, with as much as 30.4% error on average. This is illustrated in the histogram in figure 28 (i). The same is indicated in the histograms in figure 30 (i) where automatically detected diameter is compared with manual detection in 49 datasets; the diameter is mostly overestimated by the GTC criterion.
The Bland-Altman plot in figure 31 (i) illustrates the error in the detection; the points are centered around a mean value of 1.237 mm instead of 0 mm, and the points are spread out with a large *std* of 1.211 mm. In the conventional scatter plots in (ii) and (iii) it is easily seen that nearly all the diameters are overestimated as the points lie above the equality-diagonal, meaning that the detection of the anterior and/or posterior intima-lumen interfaces are detected erroneously.

This method was presented as a promising method for automatic detection of the heart wall in cardiac ultrasound [24] and for detecting the Coronary vessel wall in intravascular ultrasound [20], as explained in section 2.3.2.4. In vascular ultrasound however, this method does not seem very promising. The reason for this is probably because when imaging the Coronary vessel wall and the heart wall, there is only one hypoechoic-echogenic transition, whereas in vascular imaging with visible intimalayers, there are two hypoechoic-echogenic transitions and the media-adventitia interface has the highest gradient. It seems as the gradient part overrules the STD part in the GTC criterion, equation 19, and hence the edge is often detected to be at the media-adventitia interface.

Another issue is that it seems as the parameter tuning might have failed, as there is a lot of fluctuation in the detection. The variances in the GTC parameter tuning were large, see table 8 in appendix B.1. A high variance in the parameter tuning indicates that there will be a high variance in the detection, and this might explain why the method does not seem to work.
To overcome the problem with the gradient part of the criterion detecting the media-adventitia boundary, the $w_{std}$ was driven up, suppressing the gradient part. In addition a large window length seemed to give the best result. However, a large window length causes the weighting of the gradient part to

be even more reduced. It is the gradient that detects a leap in intensity, and so the weighting on this part should probably have been larger. What seems to be the result of trying to force the GTC to detect the intima-media layer instead of the media-adventitia layer, is an algorithm that fails completely most the time.

### 5.1.3 MMC1.5 algorithm

From visually studying figures 23 and 24, (iii) and (iv), the MMC1.5 algorithm seems to detect the correct intima-lumen boundary for both the anterior and the posterior wall. The images in figure 25 demonstrates that the algorithm often detects the wall correctly or with a small error(datasets 7, 13, 14 and 19). In some of the datasets, the algorithm fails completely to detect either the anterior or the posterior wall. In dataset 5, for example, the algorithm fails in detecting the anterior wall and instead detects on a structure further into adventita. The reason for this might be that there is a highly echogenic streak above the detected point, with another echogenic line underneath. This correlates with the model with 1.5 Gaussian curves and hence the criterion detects this to be the edge. Another reason for the erroneous detection might be that there is no echo at the crossing of the beam and the correct intima-lumen boundary, as illustrated in the same dataset, number 5 in figure 25. In other images the MMC1.5 algorithm sticks to an artifact in the lumen, for example dataset 16 in figure 25. The reason for this is probably that the artifact has a echo intensity curve that matches with the model.

Studying table 4 and the histograms in figure 28 (ii) indicates that the MMC1.5 algorithm in most cases detects the anterior wall a bit too far into the wall ($\mu_{ant}$ equals -0.438 mm and $\sigma_{ant}$ is 0.591 mm). In some datasets the detection fails completely, after removing these the bias reduces to -0.281 mm and *std* to 0.223 mm. Looking at the histogram of the detection error in the posterior wall, the MMC1.5 seems to detect the intima-lumen more correct when compared with manual detection($\mu_{post}$ is -0.041 mm and $\sigma_{post}$ is 0.582 mm). After removing the datasets where the algorithm fails completely to detect the posterior intima-lumen boundary, the edges are often detected correctly or with a slight error, (bias of -0.010 mm, and the *std* has decreased to 0.290 mm).
Excluding the cases where the detection fails completely, the MMC1.5 method seems to be more precise in the detection on the posterior than the anterior wall. This is in coherence with what was seen in the interobserver differences above, and also what is explained in the theory in section 2.2.4. The boundary is more clear in the posterior wall, as the edge is not affected by the echoes from adventitia. Therefore the intensity signature in the poste-

rior wall probably correlates more with the model than the signature in the anterior wall where the echo is affected by the pulse tail.

The detection of the vessel diameter seem to be overestimated in most cases, compared with manually detected diameter, there is a bias of 0.397 mm and *std* is 0.771 mm, see histogram in figure 28 and table 4. The reason for the diameter overestimation is that for both the anterior wall and posterior, the intitma-lumen boundary is often detected to be a bit further into the wall than the manually detected boundary. When the MMC1.5 detection fails in either the anterior, posterior or both walls, the diameter detection fails. This means that the diameter detection fails more frequently. After removing the datasets where the detection in either the anterior or the posterior wall fails completely, the *std* is reduced from 13.6% to 5.8%(0.323 mm) when relating the detection error to the actual vessel diameter.

As seen above, in some datasets the MMC1.5 algorithm fails completely to detect the wall, and sticks to either a bright structure somewhere within the wall, or an artifact in the lumen. This implies that the signature correlates with the model at these candidate points or that there is no visible intima layer at in the selected beam.

The reason why, in some dataset, both the anterior and posterior intima-lumen boundary are detected to be a bit further into the wall, compared with manual detection, could be that the candidate point might have been positioned incorrectly in the model. The candidate point was placed at what seemed correct position in the model, but this might not be in agreement with the visual boundary when looking at the ultrasound images. In other words, the model matching method might detect the edge correctly according to the model, but not in accordance with the manual detection.

The results of the comparison between automatic detected diameter and the diameter detected manually in the 49 datasets supports the results from the verification above. The histograms in figure 30 indicates that the method is good in most cases, whilst fails completely in some. The mean value of the diameter difference (MMC1.5 - manual detection) is 0.014 mm, that is a bias of 1.3% when relating to true vessel diameter. The *std* is quite large, 1.056 mm, but is reduced to 0.347 mm after removing the 12 outlays. In the Bland-Altman plot in figure 32 most of the points are positioned close to the middle value. This is also seen the conventional scatter plots in the same figure, most points are close to the equality-diagonal. Studying the conventional scatter plots one can note that diameters larger than 7 mm are all underestimated by the MMC1.5.

### 5.1.4 Issues concerning both GTC and MMC1.5

An issue when verifying the methods is that the detection was only done on one of the eight beams. These beams were selected to be good beams for manually detecting the vessel diameter in the Asklepios study. This manual selection, however, does not always correspond with the criterion for which beam is best suitable for automatic detection; that there is a clearly visible intima-lumen boundary. When testing the automatic detection on all eight beams in a dataset, the detection often works in some of the beams and fails in others. This is illustrated in figure 26, the detection on beam number 4 (the selected beam), has an intima-lumen boundary that is hardly visible and the detection fails. On the neighboring beams however, the boundaries are detected correctly. Perhaps that instead of the user selecting one beam before detecting on it, a better approach would be to do the detection on all eight beams first, followed by the user selecting the best beam to work with.

Another issue is that the AVDA is temporary, it does not look across the beams. In the methods presented by Gustavsson et al. [13] and Liang et al. [19], boundary continuity is a cost criterion. By including this criterion the edge detected on one beam coincide with the edge detected in the other beams, which prevents leaps where one beam is detected incorrect while the others are detected correctly, resulting in a smoother obtained boundary. In addition, the algorithm could be adaptive and learn from where the edge was detected on the previous beam, leading to a reduction in the search area for this beam.

The diameter verification on the 49 datasets, where comparing manually detected diameter and automatically detected diameter does not always show whether the boundary detection using the implemented criterion is done correctly. As seen from above, in both the automatic methods implemented, the detection might fail in either the anterior or posterior wall, and hence the detected diameter is incorrect and the verification on these datasets fails. It is shown above that the detection on the posterior wall is better than the detection on the anterior wall. This does not appear from the diameter verification. However, this kind of verification is good as a secondary verification method where the results support the outcome of the primary verification method.

**Computational performance**

As seen from table 6, the computational performance for MMC2 has been improved by more than 50%. The goal of improving the computational cost of the AVDA using this criterion was therefore acheived. However, both the model matching criteria are still very timeconsuming compared to the other criteria, and more work on the code will probably make it more optimal.

## 5.2 Feasability study - Brachialis

A study of the Brachialis vessel images in figures 33 and 34 was done to see whether it is possible to use the AVDA for detecting the Brachialis vessel wall and which criterion is best under these circumstances. The Transition criterion seemed to fail on all the beams in the selected datasets. The MMC1.5 and MMC2 seems to underestimates the diameter as both the anterior and posterior wall was detected a bit into the lumen. In Brachialis recordings, the intimalayer is hardly ever visible, the layer is much thinner than the intimalayer in Carotid. This makes the echo intensity signature different from the Carotid signature, hence the models in MMC1.5 and MMC2 are probably not good models for finding the vessel wall in this kind of images. The GTC criterion seems to fluctuate, it detects correctly on some beams, while fails on other. The Gradient criterion, developed by Rabben [23], however, seems to be the best criterion for a robust detection of the Brachial diameter as the detection seems to be correct on nearly all the beams in the various images.

Testing the Gradient criterion on recordings taken according to the HUNT-protocol demonstrates that it is possible to measure the diameter change during a heart cycle and it is also possible to measure the difference in diameter for the different recordings, as shown in figure 35.

# 6 Conclusion

The aim of the thesis was to develop a fully automatic algorithm that robustly identifies the carotid artery wall boundaries throughout a heart cycle. This was done by implementing two different edge detection criteria; the *GradTrans Criterion*, (GTC), and the *Model Matching Criterion with 1.5 Gaussian Curves* (MMC1.5).

The validation of the results allude the most promising of the two proposed criteria to be the MMC1.5 method. The diameter bias when comparing to manual detection is 0.014 mm, which is a mean error of 1.7% when relating to the actual vessel diameter. The *std* is quite high, 1.056 mm, 15.7% when relating to the vessel diameter. The major problem of the MMC1.5 criterion is that occasionally the algorithm fails completely; the edge is detected to be at a structure further into the wall or at an artifact in the lumen. After removing these outlays, the diameter bias increased to 0.146 mm but the *std* reduced to 0.347 mm.The algorithm has to be improved further to be more accurate, and to be more robust to overcome the problems with complete failure.

The GTC method, however, does not seem to work very promising for this purpose; the vessel diameter is overestimated in most of the datasets as the edges are detected to be within the vessel wall.

The strength of the Automatic Vessel Detection Algorithm (AVDA) is that it is fully automatic, with no user interaction required. Further development of the MMC1.5 criterion making it less time consuming and more robust, might improve the accuracy and robustness of the AVDA.

The results of the feasability study on the Brachialis vessel seems promising when using the Gradient criterion. It is possible to automatically measure diameter changes throughout a heart cycle as well as measuring the differences in diameter between recordings. This implies that the AVDA using the gradient criterion might improve the efficiency of Flow Mediated Dilation (FMD) measurements.

**Further work could include:**

- The aim of this thesis was to implement a method that function on high quality images with a visible intima-layer. It will therefore probably not provide the same results on poor images, like images of old or overweight people, where the quality of the recordings often are much lower. Further work could include expanding the AVDA to work on both high quality and low quality ultrasound images.

- As the MMC1.5 method seems to succeed in finding the correct intima-lumen interface in at least one of the eight beams, I propose that the vessel wall detection to be done on all eight beams first, and then select the most suitable beam to work with.
- Expanding the algorithm to find both the intima-lumen and the media-adventita transitions, to be able to measure both inner and outer diameter as well as intima media thickness, could be part of further work.
- Another improvement could be to integrate a criterion for boundary continuity, like proposed by Gustavsson [13] and Liang [19]. It is known that the edge should be at approximately the same depths as the neighboring beams, and hence learning between the beams could be used to improve the detection.

# References

[1] Anderson ME, Trahey GE. A seminar in k-space applied to medical ultrasound. Department of Biomedical Engineering, Duke University, 2000

[2] Angelsen B, Torp H. Forelesningsnotater SIE3065/SIE3067 Høst 2002, www.ultrasoundbook.com

[3] Asklepios study, Gent University Hospital, 2006

[4] Barth JD. An Update on Carotid Ultrasound Measurement of Intima-Media Thickness. Americal Journal of Cardiology, vol 89, pp 32B-39B, 2002

[5] Bland JM, Altman DG. Statistical Methods for Assessing Agreement Between Two Methods of Clinical Measurement. Lancet, pp 307-310, 1986

[6] Blankenhorn DH, Hodis HN, Arterial Imaging and Atherosclerosis Reversal, Arteriosclerosis and Thrombosis, vol 14, no 2, 1994

[7] Chan RC, Kaufhold J, Hemphill LC, Lees RS, Karl WC. Anisotropic Edge-Preserving Smoothing in Carotid B-mode Ultrasound for Improved Segmentation and Intima-Meida Thickness(IMT) Measurement. Computers in Cardiology, vol 27, pp 37-40, 2000

[8] Chen CH, Nakayama M, Nevo E, et al. Coupled Systolic-Ventricular and Vascular Stiffening With Age, Journal of the American College of Cardiology, vol 32, pp 1221-1227, 1998

[9] Cinthio M, Jansson T, Eriksson A, Persson Hans W, Lindstrøm K. A Robust and Fast Algorithm for Automatic Arterial Lumen Diameter Measuremen with Ultrasound. Dissertation for the degree of Ph.D., Lund University, 2004

[10] Corretti MC, Anderson TJ, Benjamin E, et al. Guidelines for Ultraound Assessment of Endothelial-Dependent Flow-Mediated Vasodilation of the Branchial Artery. Journal of the American College of Cardiology, vol 39, no 2, 2002

[11] Duck FA, Physical properties of tissue - A comprehensive reference book, ISBN Academic Press, London, 1990

[12] Edvardsen KH, Advanced measurement and analysis methods in vascular ultrasound, Department of Electronics and Telecommunications, NTNU, 2005

[13] Gustavsson T, Liang Q, Wendelhag I, Wikstrand J. A Dynamic Programming Procedure for Automated Ultrasonic Measurement of the Carotid Artery. Computers in Cardiology, 1994

[14] Hamarneh G, Abu-Gharbieh R. Implementation and Comparison of four different boundary detection algorithms for quantitative ultrasound measurements of the human carotid artery. Master Thesis, Chalmers university of Technology, 1996

[15] Heimdal Andreas, Doppler based ultrasound imaging methods for noninvasive assessment of tissue viability. Dissertation for the degree of Ph.D., NTNU, 1999

[16] Hodis HN, Mack WJ et al., The Role of Carotid Arterial Intima-Media Thickness in Predicting Clinical Coronary Events, Ann. Intern. Med. vol 128, pp 262-269, 1998

[17] Holm S, Medisinsk Ultralydavbildning, 2000

[18] Kirkhorn J, Introduction to IQ-demodulation of RF-data, NTNU, 1999

[19] Liang Q, Wendelhag I, Wikstrand J, Gustavsson T. A Multiscale Dynamic Programming Procedure for Boundary Detection in Ultrasonic Artery Images. IEEE Transactions on medical imaging, vol 19, no 2, 2000

[20] Luo Z, Wang Y, Wang W. Estimating Coronary Artery Lumen Area With Optimization-Based Contour Detection. IEEE Transactions on Medical Imaging, vol 22, no 4, 2003

[21] MSD web site, http://www.msd.no/content/pharmacists/training/training_3/no_pharama_k3_k1.html

[22] Rabben SI, Torp AH, Støylen A, et al. Semiautomatic contour detection in ultrasound m-mode images. Ultrasound in Med. & Biol., vol 26, no 2, pp. 287-296, 2000

[23] Rabben SI, GcMat toolbox for tracking and detecting arterial walls. Personal communication. 2005

[24] Rabben SI, Personal Correspondence. 2006

[25] Rabben SI, Segers P, De Backer J, et al. In vivo validation of a vessel wall tracking system based on an autocorrelation technique with RF center frequency estimation. Submitted.

[26] Scuteri A, Najjar SS, Muller DC, et al. Metabolic Syndrome Amplifies the Age-Associated Increase in Vascular Thickness and Stiffness. Journal of the American College of Cardiology, vol 43, no 8, 2004

[27] Segers P, Rabben SI, De Backer J, et al. Functional analysis of the common carotid artery: relative distension differences over the vessel wall measured in vivo. Journal of Hypertension, vol. 22, pp. 1-9, 2004

[28] Silvestrini M, Rizzato B, Placidi F, et al. Carotid artery wall thickness in patients with obstructive sleep apnea syndrome. Stroke, vol 33, pp 1782-1785, 2002

[29] Torp AH, Rabben SI, Støylen A, et al. Automatic Detection of Left Ventricular Landmarks in Echocardiography. Ultrasonics Symposium, 2004 IEEE, vol 1, pp 474 - 477, Digital Object Identifier 10.1109/ULTSYM.2004.1417765, 23-27 Aug. 2004

[30] Torp H, Crosby J, Øving 6, TTK4165 Signalbehandlingsmetoder i medisinsk billeddannelse, 2005

[31] Torp H, Crosby J, Øving 7, TTK4165 Signalbehandlingsmetoder i medisinsk ultralyd, 2005

[32] University of Oklahoma web site, Helth Sciences Center, http://w3.ouhsc.edu/histology

[33] University of Pittsburgh web site, http://www.pitt.edu/ super1/lecture/lec3281/index.htm

[34] University of Tromsø web site, http://uit.no/172/6568/9

# A Appendix A

## A.1 Displacement estimator

This is taken from [25].

The RF-signal is denoted by $s_i(z)$, where $z$ is a certain depth from the transducer and corresponds to the elapsed time after pulse transmission and $i$ is the pulse number. $s_i(z)$ is complex demodulated:

$$\tilde{s}_i(z) = LPF\Big\{s_i(Z)e^{-j2\pi f_m 2z/c}\Big\} \tag{22}$$

where $LPF.$ represents a low-pass filter, $j = \sqrt{-1}$, $c$ is the speed of sound and $f_m$ is the demodulation frequency. $\tilde{s}_i(z)$ is a low-frequency complex signal with in-phase and quadrature components(IQ data). The RF center frequency is estimated as follows:

$$\hat{f}_0 = f_m + \frac{\angle\hat{R}(1,0)}{2\pi}\tilde{f}_s \tag{23}$$

where $\tilde{f}_s$ is the sampling frequency of the complex demodulated signal $\tilde{s}_i(z)$, $\angle$ denotes the phase angle and $\hat{R}(1,0)$ is the estimate of the complex-valued correlation of $\tilde{s}_i(z)$ in the range direction. The last term on the right hand side is an estimate of the mean frequency of the quadrature demodulated signal, and corresponds to the deviation between the demodulated frequency $f_m$ and the RF center frequency. To estimate the displacement:

$$\widehat{\Delta z} = \frac{1}{2}\frac{\angle\hat{R}(1,0)}{2\pi}\frac{c}{\hat{f}_0} \tag{24}$$

where $\hat{R}(1,0)$ is a complex-valued correlation estimate of $\tilde{s}_i(z)$ at a certain depth $z$. This differs from the conventional autocorrelation method in that the demodulated frequency $f_m$ is replaced by the estimated RF center frequency $\hat{f}_0$. To determine the complex-valued correlation function $\hat{R}$ in equations 22 and 23, the sample mean estimator is used:

$$\hat{R}(m',n') = \frac{1}{M-m'}\frac{1}{N-n'}\sum_{m=0}^{M-m'-1}\sum_{n=0}^{N-n'-1}\tilde{s}_n(m)^*\tilde{s}_{n+n'}(m+m') \tag{25}$$

where $m'(\geq 0)$ and $n'(\geq 0)$are the spatial and temporal lags, while $M \times N$ is the estimation window.

# B Appendix B

## B.1 Parameter tuning

An overview of the datasets (from Datasets$_{Param}$) that are used in the parametertuning of GTC and MMC1.5.

| Filename | Beams used (b1 , b2) |
|---|---|
| rv1 | 4, 5 |
| da2 | 3, 6 |
| dh1 | 3, 4 |
| pd1 | 3, 4 |
| mv1 | 1, 2 |
| mt1 | 2, 4 |
| vt1 | 2, 5 |
| ds1 | 1, 2 |
| bh1 | 2, 6 |
| dsj1 | 2, 3 |
| me1 | 7, 8 |
| bd1 | 1, 8 |
| rp2 | 4, 6 |

**Table 7:** An overview of the datasets used for tuning the parameters; Filename and beams with visible intimalayer.

| Filename | $WL$(b1/b2) | $w_O$(b1/b2) | $w_{std}$ | %$AntAmp$ | %$PostAmp$p |
|---|---|---|---|---|---|
| rv1 | 25/27 | 0/0 | 0.9/0.9 | 40/44 | 38/39 |
| da2 | 27/NaN | 0/NaN | 0.9/NaN | 15/NaN | 32/NaN |
| dh1 | 27/27 | 0/0 | 0.9/0.9 | 47/47 | NaN/42 |
| pd1 | 27/27 | 0/0 | 0.9/0.9 | 26/21 | 65/53 |
| mv1 | 27/27 | 0/0 | 0.9/0.9 | 34/43 | NaN/NaN |
| mt1 | 27/27 | 0/0 | 0.9/0.9 | 48/58 | 51/52 |
| vt1 | 27/27 | 0/0 | 0.9/0.9 | 45/45 | 45/NaN |
| ds1 | 27/27 | 0/0 | 0.9/0.9 | 27/44 | 49/49 |
| bh1 | NaN/27 | 0/0 | 0.9/0.9 | NaN/43 | NaN/49 |
| dsj1 | 27/27 | 0/0 | 0.9/0.9 | 48/49 | 48/33 |
| me1 | 27/25 | 0/0 | 0.9/0.9 | NaN/41 | 41/44 |
| bd1 | NaN/21 | 0/0 | 0.9/0.9 | 48/40 | NaN/15 |
| rp2 | 27/27 | 0/0 | 0.9/0.9 | 23/NaN | NaN/38 |
| $\mu$ | **27** | **0** | **0.9** | **40** | **43** |
| $\sigma$ | **1.34** | **0** | **0** | **10.85** | **10.68** |

**Table 8:** An overview of the tuning of the GTC parameters; filename, window length in points ($WL$), weighting outside ($w_O$), std weighting ($w_{std}$), % amplitude of anterior wall (%$AntAmp$) and % amplitude of posterior wall (%$PostAmp$).

| Filename | $WL$(b1/b2) | $\theta_1$ (b1/b2) | %$AntAmp$ | %$PostAmp$ |
|---|---|---|---|---|
| rv1 | 21/21 | 15/10 | 46/47 | 45/50 |
| da2 | 21/NaN | 15/NaN | NaN/NaN | 48/NaN |
| dh1 | 21/21 | 15/15 | 50/42 | NaN/42 |
| pd1 | 21/21 | 10/10 | 48/52 | 52/52 |
| mv1 | 21/21 | 10/15 | 47/49 | 36/NaN |
| mt1 | 21/21 | 15/15 | 50/50 | 50/40 |
| vt1 | 21/21 | 5/5 | 50/50 | 50/50 |
| ds1 | 21/21 | 15/15 | 42/50 | 50/50 |
| bh1 | 21/21 | 10/15 | 45/48 | 45/49 |
| dsj1 | 21/21 | 15/15 | 40/40 | 40/40 |
| me1 | 21/21 | 15/15 | 35/NaN | 36/46 |
| bd1 | NaN/NaN | NaN/NaN | NaN/NaN | NaN/NaN |
| rp2 | 21/21 | 15/15 | 45/47 | 37/42 |
| $\mu$ | **21** | **13** | **46** | **45** |
| $\sigma$ | **0** | **3.28** | **4.34** | **5.44** |

**Table 9:** An overview of the tuning of the MMC1.5 parameters; filename, window length ($WL$) in points, offset value ($\theta_1$) in points, % amplitude of anterior wall (%$AntAmp$) and % amplitude of posterior wall (%$PostAmp$).

# C Appendix C

## C.1 Datasets

An overview of the 22 datasets selected from Datasets$_{Ver}$ that are used in the verification of the vessel wall detection criteria.

| Dataset | Beam | Frame (ecg-triggerpoint) | Heart cycles |
|---|---|---|---|
| 1 | 4 | 43 | 3 |
| 2 | 5 | 43 | 3 |
| 3 | 5 | 45 | 3 |
| 4 | 6 | 42 | 3 |
| 5 | 7 | 36 | 3 |
| 6 | 5 | 24 | 3 |
| 7 | 6 | 28 | 3 |
| 8 | 4 | 25 | 3 |
| 9 | 4 | 25 | 3 |
| 10 | 4 | 41 | 3 |
| 11 | 5 | 25 | 3 |
| 12 | 4 | 29 | 3 |
| 13 | 5 | 40 | 3 |
| 14 | 4 | 45 | 3 |
| 15 | 5 | 37 | 3 |
| 16 | 4 | 48 | 3 |
| 17 | 4 | 29 | 3 |
| 18 | 5 | 56 | 3 |
| 19 | 5 | 26 | 3 |
| 20 | 5 | 26 | 3 |
| 21 | 6 | 66 | 3 |
| 22 | 4 | 52 | 3 |

**Table 10:** An overview of the datasets used; Dataset number, beam used in verification, frame used in the verification (one ecg-trigger point) and number of heart cycles.

## C.2 Verification datasets

In this appendix, the visual results in datasets not presented in the results chapter are presented.

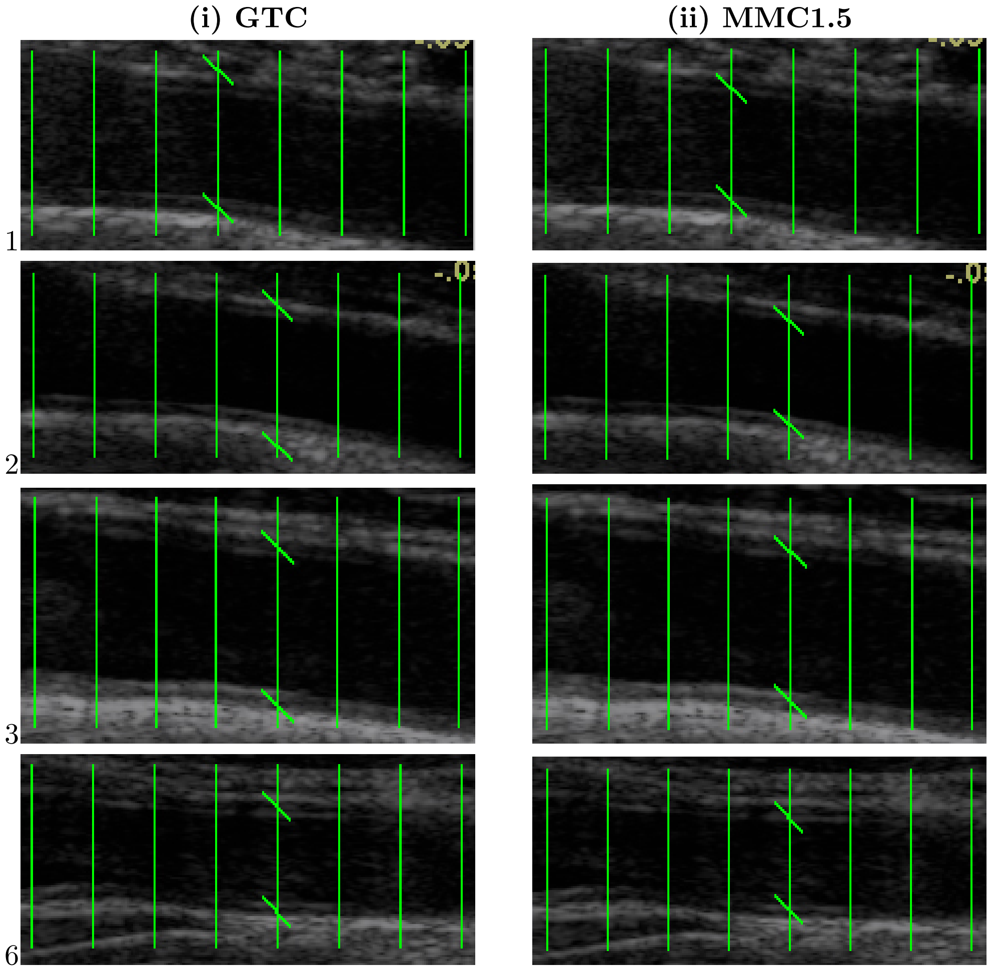

**Figure 36:** Carotid wall detection on dataset 1, 2, 3 and 6 using GTC (i) and MMC1.5 (ii) criteria.

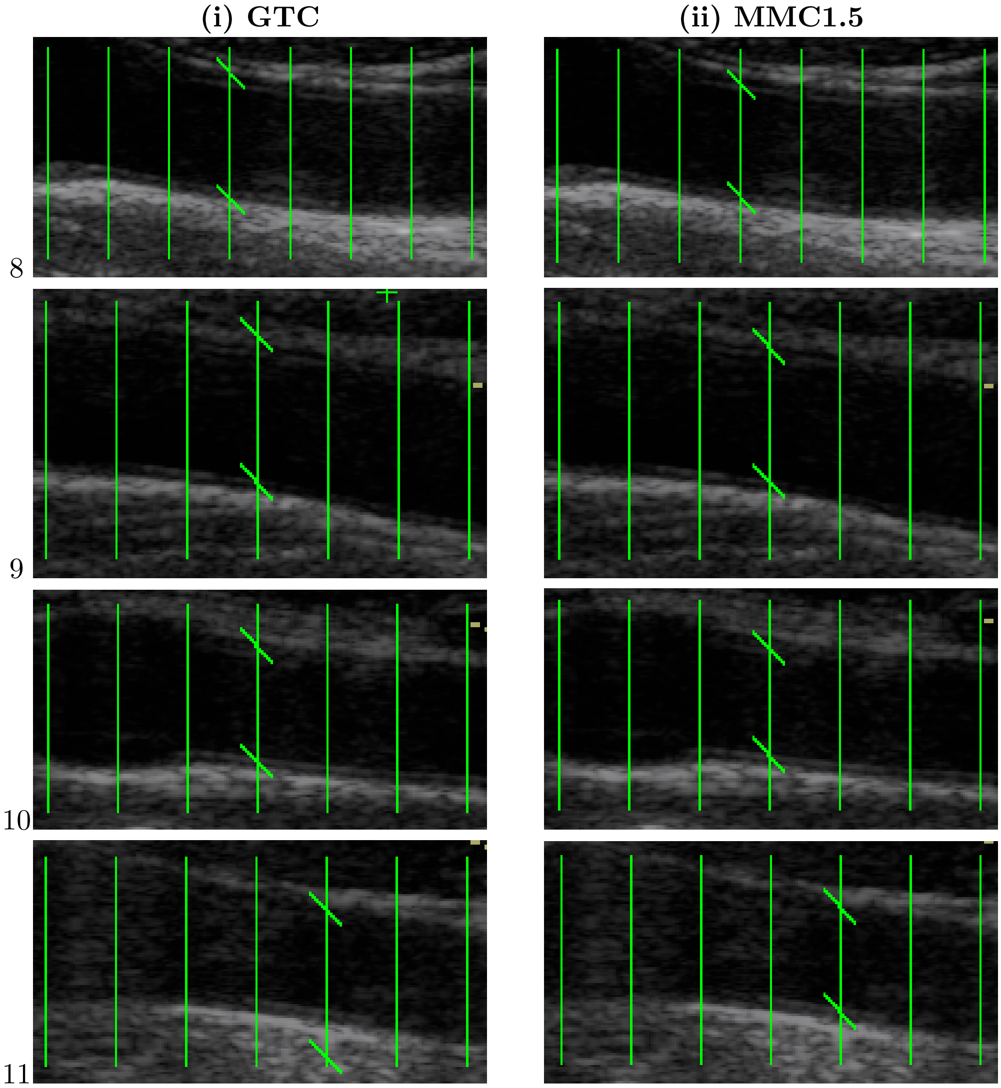

**Figure 37:** Carotid wall detection on dataset 8, 9 10 and 11 using GTC(i) and MMC1.5 (ii) criteria.

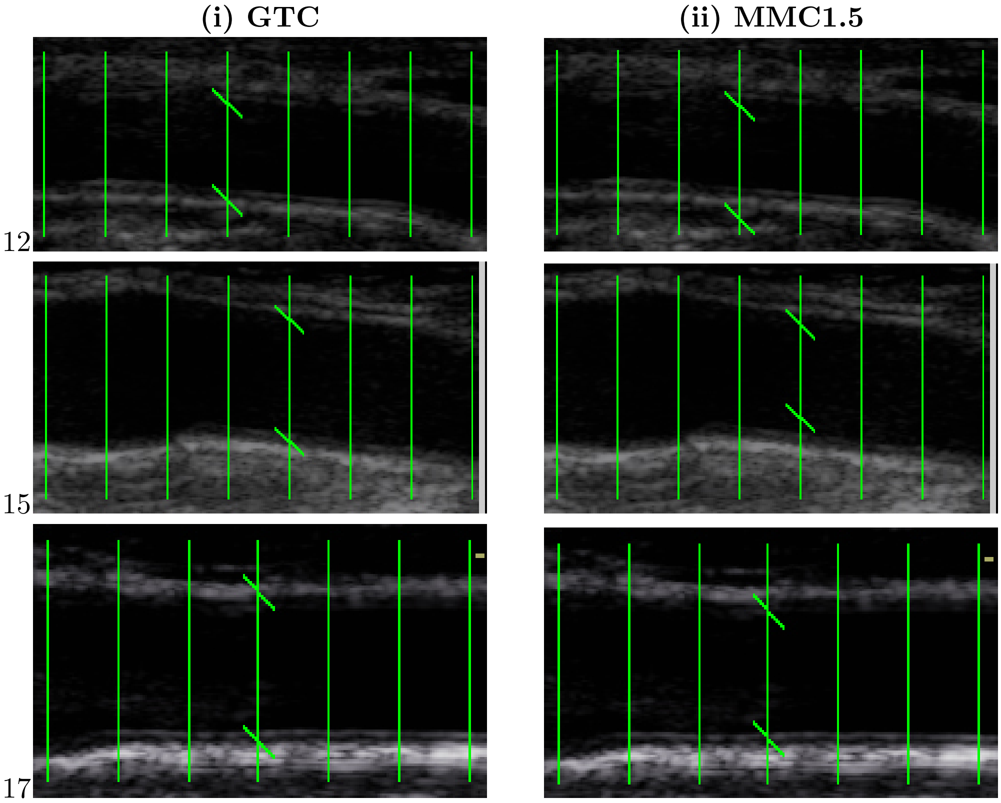

**Figure 38:** Carotid wall detection on dataset 12, 15 and 17 using GTC (i) and MMC1.5 (ii) criteria.

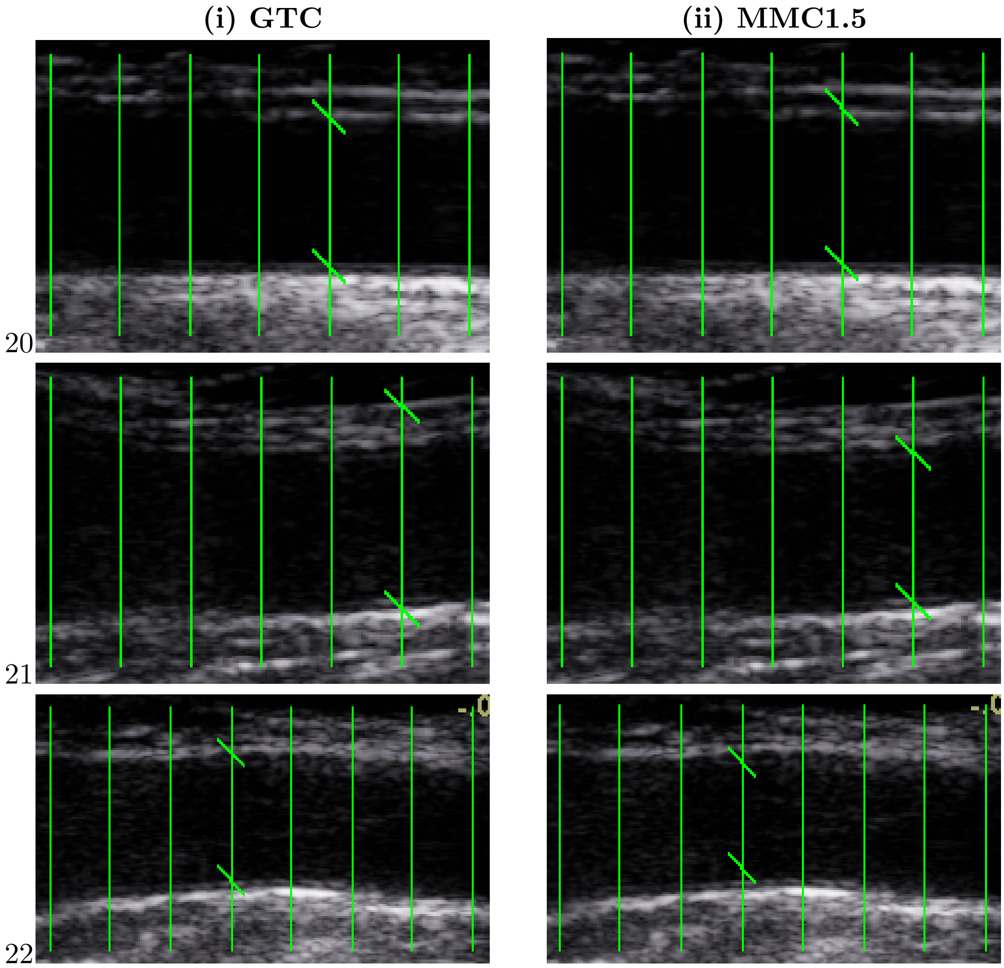

**Figure 39:** Carotid wall detection on dataset 20, 21 and 22 using GTC (i) and MMC1.5 (ii) criteria.

## C.3 Brachialis datasets

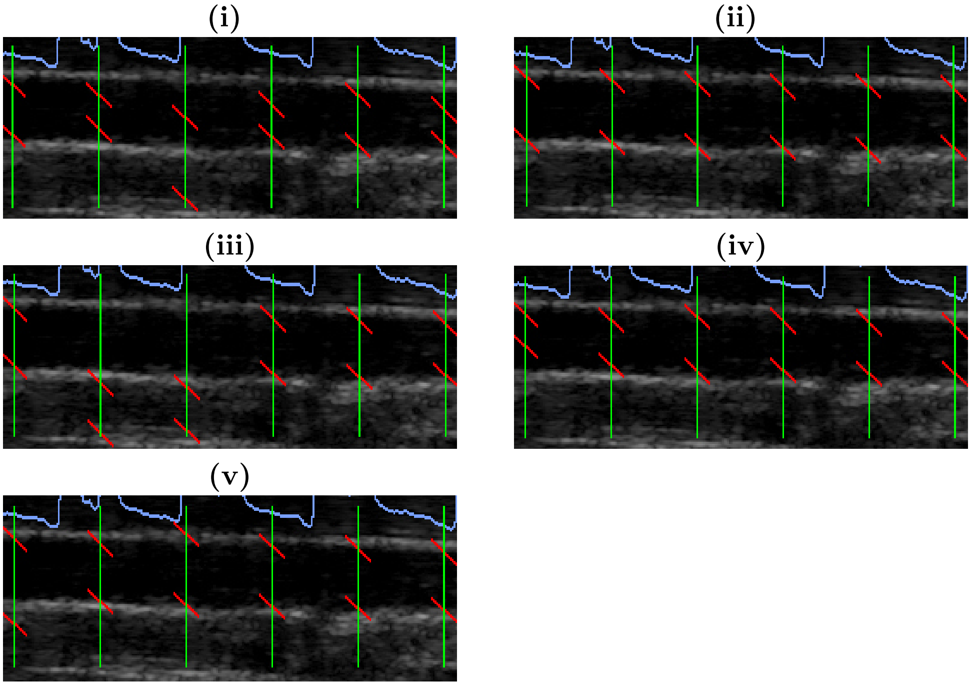

(i) (ii) (iii) (iv) (v)

**Figure 40:** Detecting the Brachialis vessel wall using the various external cost criteria: Transition (i), Gradient (ii), GTC (iii), MMC1.5 (iv) and MMC2 (v).

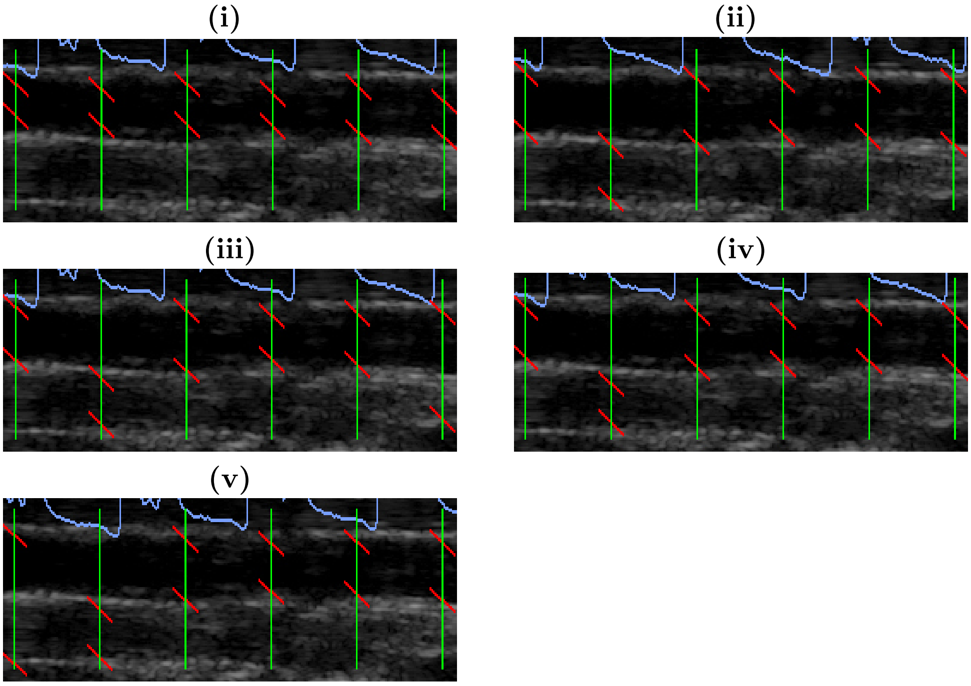

**Figure 41:** Detecting the Brachialis vessel wall using the various external cost criteria: Transition (i), Gradient (ii), GTC (iii), MMC1.5 (iv) and MMC2 (v).